

1 *This paper is a non-peer reviewed preprint submitted to EarthArXiv*

2

3

4

Title:

5

Inferring Long-Term Tectonic Uplift Patterns from Bayesian Inversion of Fluvially-Incised

6

Landscapes

7

8

Bar Oryan^{1*}, Boris Gailleton², Jean-Arthur Olive³, Luca C. Malatesta⁴ and Romain Jolivet^{3,5}

9

10 **Affiliations:**

11

(1)Scripps Institution of Oceanography, UC San Diego, La Jolla, CA 92093,USA

12

(2)Univ. Rennes, Géosciences Rennes, UMR 6118, 35000 Rennes, France.

13

(3)Laboratoire de Géologie, École normale supérieure – PSL, CNRS UMR 8538, Paris, France.

14

(4)Earth Surface Process Modelling, GFZ German Research Center for Geosciences, Potsdam,
Germany.

15

(5)Institut Universitaire de France, 1 rue Descartes, 75006 Paris.

16

17

Corresponding author: Bar Oryan (bar.oryan@columbia.edu)

18

19

20

21 **Abstract**

22 Earth surface processes encode the combined forcing of tectonics and climate in
23 topography. Separating their contributions is essential for using landscapes as quantitative
24 records of crustal deformation. Here, we develop a method for inverting spatially-variable fields
25 of long-term rock uplift and rock erodibility from fluvially-incised landscapes, while accounting
26 for climatic variability. Our approach operates in the χ reference frame and uses B-spline
27 interpolating functions to represent spatial heterogeneities in key geomorphological parameters.
28 Upon inverting 170 synthetically-generated landscapes, we demonstrate that our method
29 accurately recovers the spatial variability of key geomorphic agents, even when applied to
30 settings that deviate from the ideal model of equilibrated detachment-limited channels, which
31 underpins the χ -space framework. We subsequently apply our inversion to five natural
32 landscapes shaped by normal faults (half-grabens), and to a 200-km wide region of the Himalayas.
33 We show that our inversion can resolve the effect of climate and lithology while extracting uplift
34 fields that are consistent with patterns expected from upper crustal flexure and previous
35 estimates derived from geomorphological markers. The success of our method in recovering
36 uplift patterns, isolated from the effects of climate and erodibility, highlights its applicability to
37 settings where long-term uplift trends are unknown, paving the path to deciphering time-
38 averaged tectonic fingerprints recorded in landscapes over tens of thousands of years.

39

40

41

42

43 **Plain Language Summary**

44 Earth's topography is uniquely shaped by both deep tectonic activity and the erosive processes
45 that sculpt its surface. Utilizing these landscapes to deduce tectonic activity presents valuable
46 insights, albeit elusive. In this study, we introduce a mathematical inversion method utilizing
47 geomorphic indices to extract tectonic uplift patterns from landscapes. We assess this method's
48 effectiveness on simulated synthetic landscapes that include a variety of surface processes. Our
49 findings confirm that the method can accurately retrieve uplift rate patterns, even in landscapes
50 not solely governed by steady state detachment-limited erosion—the assumption underlying our
51 inversion technique. Applying this method to natural landscapes shaped by normal faults and the
52 Himalayas, we demonstrate that our extracted uplift patterns align with expected patterns of
53 tectonic warping. This approach sets the stage for using landscapes to decipher tectonic signals
54 accumulated over tens of thousands of years.

55

56 **Key Points**

- 57 • New method infers unknown uplift patterns and variable erodibility from fluvial
58 landscapes using a Bayesian approach.
- 59 • Synthetic tests reveal the broad applicability of our method, even when deviating from
60 the steady-state detachment-limited incision.
- 61 • Inverting six natural landscapes yields uplift fields consistent with previous estimates, or
62 patterns expected from upper crustal warping

63

64 1 Introduction

65 Earth's topography reflects a delicate balance between tectonic forcing and climate-
66 modulated surface processes. The first induces vertical motion of the surface through processes
67 such as faulting, dynamic topography and isostasy (e.g., Faccenna et al., 2019; King et al., 1988;
68 Watts, 2001) while the latter level relief by eroding bedrock and transporting/ depositing the
69 resulting sediments (e.g., Merritt et al., 2003). Thus, the shape of landscapes represents a
70 snapshot of the ever-evolving competition of these two processes (Kirby & Whipple, 2012;
71 Molnar & England, 1990; Willgoose et al., 1991).

72 Disentangling the contributions of surface processes and tectonic forces (Fig. 1) is crucial for
73 deriving insights into tectonic activities, which is a core goal of tectonic geomorphology (e.g.,
74 Armijo et al., 1996; Lavé & Avouac, 2001; Malatesta et al., 2021). Extracting spatial patterns of
75 rock uplift rates from landscapes is particularly important as it provides direct quantitative
76 constraints on the underlying tectonic mechanisms and their persistence over geological times.
77 For instance, in landscapes shaped by normal faults, spatially-varying vertical rock uplift are used
78 to estimate the effective elastic thickness of the lithosphere (Armijo et al., 1996). The shape of
79 uplift recorded along fault scarps offers insights into the slip behavior of the fault (e.g, Holtmann
80 et al., 2023). Perhaps even more critically, variations in rock uplift rates across subduction zone
81 forearcs may be used to infer the pattern of interseismic locking on the megathrust. This is
82 because the latter modulates the accumulation of inelastic strain over multiple seismic cycles,
83 which is ultimately encoded in forearc landscapes (Cattin & Avouac, 2000; Dublanchet & Olive,
84 2024; Jolivet et al., 2020; Malatesta et al., 2021; Meade, 2010; Oryan et al., 2024) .

85 Nonetheless, extracting uplift fields from landscapes is challenging especially in the absence of
86 thermochronological data or geomorphological markers. Current approaches (e.g., Castillo et al.,
87 2014; Densmore et al., 2007; Ponza et al., 2010; Su et al., 2017) often rely on the stream power
88 incision model (Howard & Kirby, 1983) utilizing a landscape metric called the steepness index,
89 k_{sn} (Wobus et al., 2006, See section 2 for definition). While useful, k_{sn} expresses the ratio of rock
90 erodibility to rock uplift and may be strongly skewed by spatial variations in rock erodibility, a
91 quantity that is difficult to constrain. Furthermore, it depends on point measurements of surface
92 slopes, which can be noisy (Boris Gailleton et al., 2021). The χ metric, which integrates upstream

93 changes in drainage area normalized by the concavity index across entire river networks, provides
94 a quantitative alternative to recover spatial variations in uplift rates from landscapes (Perron &
95 Royden, 2013). Previous work has employed the χ metric for landscape inversion focusing on
96 uplift rate history, while neglecting or prescribing variations in uplift shape (Croissant & Braun,
97 2014; Fox et al., 2014; Goren et al., 2014; Goren et al., 2022; Pritchard et al., 2009; Smith et al.,
98 2024).

99 Here we extend the χ coordinate framework and invert landscapes for an unknown
100 (steady) field of rock uplift rate and variable spatial erodibility while including precipitation
101 patterns. To that end, we use a Bayesian quasi-Newton inversion scheme which optimizes
102 erodibility and uplift shapes parameterized by B-spline interpolation functions in a manner that
103 minimizes the misfit between measured and inverted elevation (Fig. 1). We test the strengths
104 and limitations of our method using synthetic landscapes and demonstrate its ability to recover
105 uplift shapes and erodibility coefficients while accounting for climatic effects. Subsequently, we
106 apply our method to six natural landscapes shaped by divergent and convergent tectonics to
107 demonstrate its effectiveness in real-world scenarios.

108

109 2 Inferring tectonic uplift from landscapes within the stream power 110 framework

111 2.1 The detachment-limited stream power model

112 The stream power incision model posits that the erosion rate of a riverbed at a certain
113 point is linked to water flux (captured by proxy with drainage area A), channel slope ($\frac{dz}{dx}$) and the
114 erodibility of the material (K) (Hack, 1973; Howard & Kerby, 1983). To maintain a uniform rate of
115 erosion, the river gradient diminishes downstream as drainage area increases, resulting in a
116 familiar concave river profile. According to this model, the change in elevation over time t , of a
117 river eroding at rate, E , under rock uplift, U , is described as follows:

118

119 1.
$$\frac{\partial z(x,y,t)}{\partial t} = U(x, y, t) - E(x, y, t) = U(x, y, t) - K(x, y, t)A(x, y, t)^m \left(\frac{\partial z}{\partial x}\right)^n$$

120

121

122 Where m and n are constants and (x,y) is position, hereafter denoted as \vec{x} for concision.

123 The velocity at which a change in uplift rate travels upstream as a knickpoint is linked to local
124 erodibility, drainage area and topographic gradient (Rosenbloom & Anderson, 1994; Whipple &
125 Tucker, 1999):

126

127
$$2. \quad c(\vec{x}) = k(\vec{x})A(\vec{x}) \left(\frac{dz(\vec{x})}{dx} \right)^{n-1}$$

128 The time for a perturbation to travel from the river base upstream to point x_s is defined as follows
129 (Whipple & Tucker, 1999):

130

131
$$3. \quad \tau(x_s) = \int_0^{x_s} \frac{dx}{c(\vec{x})} = \int_0^{x_s} \frac{dx}{k(\vec{x})A(\vec{x}) \left(\frac{dz(\vec{x})}{dx} \right)^{n-1}}$$

132

133 When erosion and uplift rates are balanced, the steady-state equation describes the equilibrium
134 slope of the river with an inverse power-law relationship between channel slope and drainage
135 area:

136

137
$$4. \quad \frac{dz}{dx} = k_{sn} A(\vec{x})^{-\frac{m}{n}}$$

138

139 Where $k_{sn} = \left(\frac{U(\vec{x})}{K(\vec{x})} \right)^{\frac{1}{n}}$ a quantity often normalized with respect to regional concavity value,
140 $\theta_{ref} (= \frac{m}{n})$ and used as a proxy of uplift to erosion ratio.

141

142 2.2 The integral approach: river profiles in χ -space

143

144 Upstream integration of equation 4 from an arbitrary base level x_b results in (Perron &
145 Royden, 2013):

146

$$5. \quad z(\vec{x}) = z(x_b) + a_s \cdot \chi(\vec{x})$$

147 Where,

148
$$6. \chi = \int_{x_b}^x \frac{dx}{A^*(\vec{x})^{\frac{m}{n}}}; a_s = \left(\frac{U_0}{K_0 A_0^m} \right)^{\frac{1}{n}}$$

149 and A_0 is a constant reference drainage area such that $A^*(x) = \frac{A(x)}{A_0}$ is dimensionless. The
150 integral along x here denotes an upstream path to a connected network of tributaries.

151 This coordinate transformation allows us to describe river profiles in terms of χ and z (Fig.
152 1). In the case of spatially uniform U and K , stream profiles in χ -space will exhibit a linear
153 relationship between the two variables, characterized by a slope a_s . In landscapes where
154 erodibility and uplift vary spatially, the definition of χ can be amended as (Olive et al., 2022;
155 Perron & Royden, 2013) :

156

157
$$7. \chi_{u,k} = \int_{x_b}^x \left(\frac{U^*(\vec{x})}{A^*(\vec{x})^m K^*(\vec{x})} \right)^{\frac{1}{n}} dx; a_s = \left(\frac{U_0}{K_0 A_0^m} \right)^{\frac{1}{n}}$$

158

159 In this case, U_0 and K_0 are reference values so the trailing terms are dimensionless ($U^* = \frac{U}{U_0}$,
160 $K^* = \frac{K}{K_0}$). $\chi_{u,k}$ denotes a version of χ corrected for known spatial variations in uplift rate and
161 erodibility. If $U^*(\vec{x})$ and $K^*(\vec{x})$ are properly accounted for, the steady state landscape should verify
162 equation (5) and elevation correlate linearly with $\chi_{u,k}$ (Fig. 1).

163

164 3 Inverting uplift shapes from river incised landscapes

165 3.1 Forward model

166 3.1.1 Parameter space, data space and cost function

167

168 The detachment-limited stream power model in χ -space provides a robust framework to
169 invert uplift shape from river incised landscapes. Let us begin by outlining the direct (forward)
170 problem of river profiles in χ -space, from knowledge of the parameters $m, n, a_s, U^*(\vec{x})$ and
171 $K^*(\vec{x})$. This is done by computing $\chi_{u,k}$ (eq. 7), and modeled river elevation, z_m , using eq. 5, as:

172

173
$$8. z_m = z_b + a_s \cdot \chi_{u,k}(m, n, U^*, K^*) = g(a_s, m, n, U^*, K^*)$$

174

175 We estimate the robustness of our direct model, expressed through the function g , by computing
176 the difference between modeled elevation, z_m , and measured elevation, z , using the cost
177 function, ϕ , using the L2 norm:

178

179
$$9. \phi(m, n, a_s, U^*, K^*) = ||g(a_s, m, n, U^*, K^*) - z||_2$$

180

181 Where z is the elevation data, typically obtained from a digital elevation model (DEM).

182

183 3.1.2 Parameterizing uplift patterns using B-spline functions

184

185 We parameterize the spatial variability of uplift, $U^*(\vec{x})$, using B-spline functions (De Boor,
186 1978; Piegl & Tiller, 1997). Constructed from a series of piecewise polynomial basis functions and
187 defined between a grid of control points known as knots, B-splines serve as interpolating
188 functions where a coefficient, Q , at each knot controls the shape of the uplift pattern (See Text
189 S1). This approach provides the flexibility to modify uplift patterns by simply adjusting Q values
190 without being restricted to a predetermined functional form, thus ensuring a smooth and
191 continuous representation of spatial variability in rock uplift. It is important to highlight that we
192 solve for the uplift pattern rather than the absolute uplift rate, as we cannot independently
193 determine the value of the normalization constant U_0 (eq. 7).

194

195 3.1.3 Parameterizing spatial Erodibility

196

197 Spatial variations in erodibility are typically driven by contrasts in lithology (Campforts et
198 al., 2020; Ellis & Barnes, 2015; B. Gailleton et al., 2021; Harel et al., 2016), often marked by the
199 occurrence of major faults. Thus, using continuous mathematical functions, such as B-splines,
200 polynomials, or Gaussians, to represent variations in erodibility would misrepresent the
201 inherently piece-wise nature of this field. We instead delineate lithological units (e.g., from

202 geological maps) and invert for their piece-wise uniform erodibility k_i across various lithological
203 domains (numbered by i). As for the uplift pattern, it should be noted that we invert for relative
204 erodibility K^* rather than for absolute erodibility.

205

206 3.1.4 Parameterizing climatic modulation of erosion

207

208 We account for climate-driven variations in stream power incision by weighting the
209 drainage area with precipitation rates and computing an effective volumetric discharge, $A_Q(x)$.
210 This method is commonly employed in fluvial topographic analysis to assess the impacts of
211 variable precipitations, both spatially and temporally (Babault et al., 2018; Leonard et al., 2023;
212 Leonard & Whipple, 2021). The adjusted discharge, $A_Q(x)$, at point x is defined by integrating the
213 drainage area, A , weighted by the precipitation rate, P , from the river source, x_s , downstream
214 to the base:

215

$$216 \quad 10. A_Q(x) = \int_{x_b}^{x_s} P(x)A(x)dx$$

217

218 3.2 Inversion scheme

219

220 To identify plausible combinations of a_s, m, n, U^* and K^* , we minimize the misfit
221 between the modeled and measured elevation (eq. 9) using a Bayesian quasi-Newton scheme
222 (Tarantola, 2005) in an iterative fashion:

223

$$224 \quad 11. p_{l+1} = p_l + \mu(G_n^t C_D^{-1} G_n + C_M^{-1})^{-1} (G_n^t C_D^{-1} (z_m - z_{obs}) + C_M^{-1} (p_l - p_0))$$

225

226 Where p_l is a vector comprising all model parameters at iteration l . G_n is the Jacobian
227 matrix determined using centered finite difference such that:

228

$$229 \quad 12. G_n = \frac{\partial g}{\partial p}$$

229

230 z_{obs} is a vector of observations consisting of measured elevation z , z_m is the modeled elevation
231 of rivers computed using $g(p_l)$, C_M is the a priori covariance matrix, C_D is the observation
232 covariance matrix, and μ is a constant between 0 and 1. We employ an initial guess, p_o , assuming
233 $m=0.5$, $n=1$, $a_s = 0.1$ as well as B-spline and erodibility coefficients that describe uniform uplift
234 and erodibility patterns.

235 We configure the covariance matrix C_m with diagonal terms equal to 0.01 (standard
236 deviation of 0.1) for the entries corresponding to m , n , and a_s , and 1 for B-spline weights and
237 dimensionless erodibility coefficients, reflecting a lack of a priori knowledge about spatial
238 variability in the uplift and erodibility patterns. We consider a solution m_l satisfactory when
239 $\frac{\phi(p_{l+1}) - \phi(p_l)}{\phi(p_o)} < 0.01$.

240 Upon reaching an optimal solution, we can use the recovered B-spline parameters to
241 describe the uplift pattern along rivers used in the inversion as well as across the entire
242 rectangular domain bounded by the river network (Text S1). However, the geometry of the river
243 network may leave some B-spline knots poorly constrained due to the absence of nearby rivers.
244 To address this, we compute uplift only within catchments feeding the rivers used in our analysis
245 and ensure that the employed knots have non-negligible values based on the sensitivity
246 parameter computed using the diagonal of the product of $(G_n^t \cdot G_n)$.

247

248 4 Application to synthetic landscapes

249

250 We assess the reliability of our methodology, which inherently assumes steady-state
251 incision of channels, across a range of synthetic landscapes. These artificial terrains exhibit
252 varying degrees of deviation from the stream power law and include hillslope diffusion, sediment
253 deposition, orographic effects, spatial changes in erodibility, and temporal shifts in uplift rates
254 (e.g., Leonard & Whipple, 2021; Merritt et al., 2003; Roering et al., 1999, 2001; Whipple, 2009).

255

256 4.1 Generating synthetic landscapes

257

258 We model synthetic terrains, incorporating both fluvial and hillslope erosion along with
 259 deposition dynamics based on the CIDRE model framework defined by (Carretier et al., 2016). In
 260 this framework, elevation z varies in time such as

261

$$262 \quad 13. \frac{dz}{dt} = \dot{d}_f - \dot{e}_f + \dot{d}_h - \dot{e}_h + U(x, y)$$

263

264 where \dot{d}_f is the fluvial deposition rate, \dot{e}_f the fluvial incision rate, \dot{d}_h the hillslope diffusion flux,
 265 \dot{e}_h the hillslope erosion rates and $U(\vec{x})$ is the imposed tectonic uplift. The fluvial component relies
 266 on a formulation originally developed by Davy & Lague (2009) where erosion and sediment
 267 entrainment are functions of stream power and sediment length deposition. The hillslope laws
 268 are a hybrid between linear and non-linear landscape diffusion models, reproducing both end-
 269 members (see Carretier et al., 2016 for full details).

270 We use an explicit finite difference numerical scheme to solve equation (13) where spatial
 271 discretization is done along a 100 X 100 km regular 2D grid with 400 m spacing in the x and y
 272 directions. We use different graph theory algorithms to organize our nodes into an upstream to
 273 downstream topological order (see Gailleton et al., 2024 where full method description is given)
 274 and use the carving algorithm of Cordonnier et al., (2019) to resolve local minima. We employ a
 275 time step of 500 years and run synthetic models over 5 million years to ensure the landscape
 276 reaches a topographic steady state, resulting in negligible elevation variations over time. Lastly,
 277 we use $n = 1$, $m = 0.45$ and rock erodibility, k , of $2 \cdot 10^{-5} m^{(0.9)} \cdot yr^{-1}$. We parameterize the
 278 imposed tectonic uplift field using an asymmetrical 2D Gaussian- function:

279

$$280 \quad 14. U(x, y) = u_0 \cdot \exp [-a(x - x_0) + 2b(x - x_0)(y - y_0) + c(y - y_0)^2]$$

281

282 Where $a = \frac{\cos^2(\theta)}{2\sigma_x^2} + \frac{\sin^2(\theta)}{2\sigma_y^2}$, $b = -\frac{\sin(2\theta)}{4\sigma_x^2} + \frac{\sin(2\theta)}{4\sigma_y^2}$, $c = \frac{\sin^2(\theta)}{2\sigma_x^2} + \frac{\cos^2(\theta)}{2\sigma_y^2}$, θ is the azimuth of the
 283 long-axis of the Gaussian, x_0 , σ_x and y_0 , σ_y are the center and width of the gaussian along the x
 284 and y directions, respectively. Lastly, we assume a characteristic uplift rate, u_0 , of $1.2 mm \cdot$
 285 yr^{-1} (Fig. 2).

286

287 4.2 Inversion of synthetic landscapes

288 We apply our inversion scheme on simulated synthetic landscapes and select the 8000
289 most downstream nodes from the largest catchments to guarantee our inversion outputs are not
290 secondarily influenced by the number of observations (z_{obs}). To mimic the uncertainty in real
291 elevation data we add noise using randomly sampled values from a normal distribution centered
292 around 0 with standard deviation, ε , of 10 m. We then invert the resulting landscapes using two
293 different schemes. The first solves for 84 parameters including m, n, a_s and the control points for
294 spatially-varying uplift with a 2D cubic B-spline function along 6 knots in the y and x direction.
295 The second assumes a uniform uplift pattern and fits landscape constants m, n and a_s only (eq.
296 6). We estimate how well the inversions perform by comparing recovered uplift and elevation
297 with synthetic modeled elevation and imposed uplift using the root mean square (RMS) metric:

298

299

$$15. RMS = \sqrt{\frac{1}{N} \sum_{i=0}^N (q_i^r - q_i^m)^2}$$

300 Where q_i^r is recovered value i , q_i^m imposed value i and N total number of measurements
301 in the dataset.

302

303 4.3 Results

304 4.3.1 Detachment-limited scenario

305 We produce a synthetic landscape subject to an ellipsoidal uplift function (Table S1; Fig. S1)
306 where erosion is exclusively detachment-limited (Fig. 2A). Once at steady state, we measure the
307 landscape's drainage area, flow direction, and the distance between river nodes required for
308 computing χ . We then use these landscape properties and apply two inversion mechanisms: (1)
309 solving for uplift pattern, and (2) assuming uniform uplift.

310 Our first inversion performs well, retrieving outputs that are almost identical to those imposed.
311 The RMS value for uplift is 0.01, indicating that the inverted uplift for the 8,000 river nodes used
312 closely matches the imposed tectonic uplift (Fig. 2). Additionally, our inverted elevation closely
313 mirrors the measured elevation, with discrepancies reflecting the introduced noise, ε , leading to

314 an RMS value of 10 meters. This accuracy is illustrated nicely by the linear shape of the final river
315 elevation profiles in χ -space, a_s , where the scatter reflects the noise (Fig. 2C). In contrast, the
316 inversion assuming uniform uplift returns RMS values that are 7 times higher and fails to
317 accurately determine landscape constant m, n and a_s (Fig. 2C).

318 Once we have established that our inversion can accurately recover landscape properties
319 in this idealized case, we proceed to test its limitations by challenging the assumptions it relies
320 on.

321

322 4.3.2 Scenarios deviating from the Detachment-limited endmember

323 4.3.2.1 *Sediment transport length*

324 We apply our inversion scheme to synthetic landscapes featuring varying degrees of
325 sediment deposition, hillslope diffusion, orographic effects, spatial variations in erodibility, and
326 temporal changes in uplift rates. For the sediment deposition case, we generate 20 identical
327 landscapes, differing only in the value of the characteristic sediment transport length (e.g.,
328 Carretier et al., 2016; Merritt et al., 2003). For transport lengths longer than 1 km, our inversion
329 accurately recovers landscape parameters with RMS elevation and uplift values comparable to
330 the noise we added, ε (Figs. 3A1 & 3B1). Landscapes characterized by transport length shorter
331 than 1 km generate greater relief owing to the additional sediment deposition. Consequently,
332 inverting these models yields less accurate inversion results, with RMS values 5 to 30 times higher
333 for both elevation and uplift (Figs. 3A1 & 3B1). Interestingly, even as the landscape deviates
334 significantly from the detachment-limited case, the inversion aims to maintain the imposed $\frac{m}{n}$
335 ratio, capturing this "detachment-limited property" of the landscape (Fig. S2).

336

337 4.3.2.2 *Diffusion*

338

339 To test the effect of hillslope diffusion on our inversion, we model and invert 50 landscapes,
340 each employing a distinct diffusion parameters k_d controlling topographic dispersion across the
341 landscapes (Carretier et al., 2016). For k_d smaller than $10^{-2} m \cdot yr^{-1}$ the inversion outputs
342 almost perfectly retrieved the parameters of the landscape (Figs. 3A2 & 3B2). For higher diffusion

343 values of $10^{-2} - 10^{-1} m \cdot yr^{-1}$, the retrieved uplift function exhibits pronounced uncertainties
344 but can still capture the original signal (Fig. S3). For $k_d > 10^{-2} m \cdot yr^{-1}$, the river network ceases
345 to represent a typical mountain range drainage system (Fig. 3B2). This is reflected in the poor
346 performance of the inversion showing RMS values 10-30 times higher than the best retrieval
347 values, partly due to the lack of river nodes in the center of domain (Fig. 3A2).

348 4.3.2.3 Precipitation

349 Spatial variability in climatic conditions can also significantly influence landscapes (e.g.,
350 Molnar & England, 1990), particularly in mountain ranges with orographic precipitation on the
351 windward flanks and drier conditions on the leeward sides (e.g., Bookhagen & Burbank, 2010).
352 To incorporate this effect into the evaluation of our synthetic models, we index precipitation on
353 elevation using the equation $p(z) = \alpha_o e^{-\frac{z}{h_0}}$, where α_o is precipitation at sea level, Z elevation,
354 and h_0 a reference elevation (Hergarten & Robl, 2022). To reflect reduced rainfall along the lee
355 side of the landscape we reduce the α_o value there, effectively generating uneven precipitation
356 $p(x, z)$ (e.g., Figs. 3B3, S3D1 and S3D2). We then simulate 50 landscapes using the effective
357 volumetric discharge A_Q (eq. 10), modulated by precipitation $p(x, z)$ with each terrain
358 characterized by a distinct h_0 .

359 Our inversion assuming that water discharge simply scales with only drainage area (A)
360 accurately recovers landscape parameters for $h_0 < 0.5$ km. For h_0 values above 0.5 km, retrieval
361 inaccuracies increase, worsening with larger values (Figs. 3A3 & 2B3). However, when we use A_Q
362 (eq. 10) in our inversion, it accurately retrieves the correct landscape parameters, effectively
363 determining elevation, uplift (Fig. 3A3), and m , n and a_s (Fig. S3). The ability of our inversion to
364 accurately retrieve landscape parameters is particularly noteworthy given that A_Q undergoes
365 significant changes as the landscape evolves with time and we use the values from the final
366 timestep.

367 4.3.2.4 Lithology

368 Lithology is an additional spatially variable parameter influencing landscape evolution.
369 We explore its significance by modeling 50 landscapes each featuring a 20 km wide zone with low
370 erodibility, k_s , varying by up to an order of magnitude from the background erodibility, k_w , $2 \cdot$
371 $10^{-5} m^{(0.9)} \cdot yr^{-1}$. The sharp change in erodibility results in landscapes with two distinct

372 topographic highs: one aligned with the imposed uplift pattern and another associated with the
373 low erodibility zone where the ratio of altitudes between these peaks is linked to $\frac{k_w}{k_s}$ (e.g., Figs.
374 3B4, S5D1 and S5D2).

375 For $\frac{k_w}{k_s} > 0.5$ our standard inversion performs well, almost unaffected by the addition of
376 a stronger rock section (Fig. 3A4). However, for $\frac{k_w}{k_s} < 0.5$, the standard inversion scheme
377 struggles to accurately capture the current properties of the landscape, and the retrieved uplift
378 values reflect the region of lower erodible domain rather than the imposed uplift shape (Fig.
379 3A4). However, when we invert for erodibility (see section 3.1.3) as well as U^* , m , n and a_s the
380 inversion scheme excels in accounting for elevation and uplift pattern (Figs. 3A4 and S5). The
381 recovered and imposed erodibility ratio are in remarkably good agreement (Fig. 3A4) suggesting
382 that our inversion scheme is capable of accounting for spatial changes in rock erodibility.

383 4.3.2.5 *Rock uplift rate*

384 To investigate the impact of time-varying tectonic forcing, we bring a detachment-limited
385 landscape to a steady state and then instantaneously increase the uplift rate by a factor of three,
386 similar to observed changes in uplift history along normal fault systems (e.g., Goren et al., 2014;
387 Smith et al., 2024). We proceed to simulate the landscape for an additional 1.6 million years until
388 it reaches a new equilibrium (calculated using Equation (3) ;Fig. S6) and invert landscapes
389 snapshots retained at intervals of 0.1 million years.,

390 Our inversion responds to the step change in uplift rate with a minor increase in RMS
391 values for the retrieved elevation. Conversely, the inversion shows greater deviations in the
392 recovered uplift pattern and in the m , n and a_s values than in elevation (Figs. 3A5, 3B5 & S7). This
393 is because the inversion effectively compensates with adjustments in other parameters to return
394 accurate elevation values. This illustrates the challenge of determining whether a natural
395 landscape is in steady state based solely on elevation errors. After about half the time needed to
396 reach equilibrium, the inversion returns values that align well with the imposed parameters (Fig.
397 3A5). This stabilization in parameter retrieval is clearly illustrated by a_s values (incorporating the
398 updated u_0 value) which reach their new steady-state levels approximately 0.8 million years after
399 the step change. We attribute the inversion's ability to retrieve the imposed values before the

400 entire landscape reaches steady state to the fact that a significant portion of the landscape is
401 already in equilibrium, with only the upstream sections of rivers still in transition. This is
402 evidenced by the large misfit values at the river tips, which, unlike in steady-state conditions, are
403 more evenly distributed across the landscape (Fig. S8). We note that we observe a similar pattern
404 in landscapes subjected to temporal changes in uplift pattern over a given time period (Text S2
405 & Fig. S8).

406

407 5 Application to natural landscapes

408 5.1 Selection of sites

409

410 To test the real-world applicability of our inversion scheme, we apply it to both divergent and
411 convergent tectonic settings. For the divergent setting, we analyze five landscapes shaped by
412 normal faults, where our understanding of the crust's flexural response to faulting provides a
413 reliable test bed for comparing our inverted uplift patterns. For the convergent setting, we focus
414 on a well-studied, approximately 200 km-wide section of the Himalayas and compare our results
415 to previous uplift estimates derived from geomorphological markers.

416

417 5.1.1 Landscapes shaped by normal faults

418

419 We apply our inversion methodology to natural landscapes shaped by half-graben border
420 faults where fault offsets on the order of several km flex the brittle upper crust, yielding a 1-D
421 rock uplift field that decreases with across-strike distance from the fault (Fig. S10; Weissel &
422 Karner, 1989). Thicker and stronger faulted layers typically produce longer uplift decay lengths,
423 extending further into the footwall. This relatively simple pattern makes it an appealing
424 benchmark case, and has been leveraged in previous geomorphological tectonic studies (e.g.,
425 Goren et al., 2014; Ellis & Barnes 2015). Recovering systematic trends in the uplift shape
426 consistent with flexural properties of several landscape would provide additional constraints on
427 the validity of our inversion.

428 To this end, we study five landscapes with varying faulted layer thicknesses (Table S2; Olive
429 et al., 2022): The Paeroa Range (Paeroa fault ,New Zealand), Sandia Mountains (New Mexico,
430 USA), Wassuk Range (Nevada, USA), Lehmi Range (Lehmi Fault, Idaho, USA), and Kipengere Range
431 (Livingstone Fault, Lake Malawi, Tanzania). We analyze river sections located far from fault tips
432 (Densmore 2007; Ellis & Barnes, 2015), ensuring that uplift is predominantly a function of
433 distance from the fault, allowing us to use the faster 1D inversion. However, to demonstrate the
434 applicability of our 2-D inversion scheme, we apply it to the Lemhi range where we specifically
435 focus on the southern section near the fault tip because its uplift pattern is well-documented and
436 has been shown to diminish southward (Fig. S10; Densmore et al., 2007).

437 We include erodibility variations for the N-S striking Sandia mountains, as they feature two
438 clear and distinct lithological domains comprising predominantly limestone on the Eastern side
439 and granite on the Western side (Williams & Cole, 2007), which typically show different erosional
440 properties (Fig. 4C2). We assume uniform erodibility in other studied landscapes as these exhibits
441 relatively uniform lithology. We do not account for spatial changes in precipitation here. The
442 Kipengere Range shows little evidence of a correlation between precipitation and altitude in
443 documented rainfall trends in the past 23 years (Fig. S11; Global Precipitation Measurement;
444 GPM; Huffman et al., 2015) despite its 1.5 km relief and an expected strong orographic effect.
445 This suggests that orographic effects may be even less important in the other gentler landscapes.

446

447 5.1.2 The Himalayas

448

449 We apply our inversion scheme to a well-studied, approximately 200 km-wide section of
450 the Himalayas, where previous studies have identified high uplift rates occurring around 100 km
451 from the main Himalayan thrust, with slower uplift rates observed farther away (Dal Zilio et al.,
452 2021; Godard et al., 2014; Lavé & Avouac, 2001). We exclude the Siwalik Hills from our analysis
453 as rivers in this region are not predominantly detachment-limited. We also omit catchments
454 north of the Himalayan water divide extending to the Tibetan Plateau, as these require separate,
455 higher base levels, which would limit the spatial extent of our analysis.

456 Our inversion accounts for four distinct erodibility sections, delineated by the main
457 lithological units in the area (Fig. 5C; Carosi et al., 2018). To incorporate the pronounced climatic
458 patterns in the Himalayas (e.g., Bookhagen & Burbank, 2010), we compute A_Q using eq (10),
459 based on the average spatial distribution of the past 23 years of satellite-based precipitation data
460 (Fig. 5D; Huffman et al., 2015).

461

462 5.2 Inversion of natural landscapes

463

464 We use 30 m-DEM of landscapes obtained by the Shuttle Radar Topography Mission (Farr
465 et al., 2007) . We extract nodes (pixels) corresponding to major rivers, defined as those draining
466 areas larger than a set threshold and above a set base level elevation (Table S2). These thresholds
467 are carefully selected to balance computational efficiency for the inversion calculations with an
468 accurate representation of the landscape’s fluvial sections. For landscapes shaped by normal
469 faults, our aim is to include river nodes that cover the entire decay length of the fault-induced
470 uplift. However, this is often complicated by river nodes near the fault, which are typically located
471 on hanging wall-facing cliffs that drain small areas or lie underwater. Consequently, we calculate
472 the rivers’ distance from the outlet, drainage area, and elevation (O’Callaghan & Mark, 1984),
473 and rotate their geographical coordinates to align with an along-fault strike and across-fault
474 strike coordinate system. We estimate their connectivity and flow path using the steepest
475 descent algorithm (O’Callaghan & Mark, 1984).

476 We compute multiple inversion scenarios for each landscape, varying the number of B-
477 spline nodes, ensuring the distance between B-spline nodes is at least 5km (Text S1). We report
478 the inversion that minimizes the Akaike Information Criterion (AIC) (Akaike, 1974; Bishop, 2006).
479 The AIC includes a penalty term to prevent potential overfitting caused by the addition of
480 superfluous parameters to the model (Text S3). We also assume an elevation uncertainty of 30
481 meters, a value that has been deliberately increased from the reported SRTM dataset
482 uncertainty. This additive inflation addresses our model’s limitations in capturing detailed terrain
483 features, as highlighted in the synthetic inversion cases. Employing such an approach is common
484 practice across various parameterizations in physical modeling, aiming to better represent the

485 inherent uncertainties without exhausting every detail (e.g., Anderson, 2007). Lastly, we note
486 that for the Malawi landscape case, we set the covariance matrix to values of 10^{-4} (standard
487 deviation of 10^{-2}) for m and n . This adjustment was necessary to avoid inverted m and n values
488 that produced unrealistically long knickpoint travel times (eq. 3).

489

490 5.3 Results

491 5.3.1 Landscapes shaped by normal faults

492

493 Our 1D inversions consistently reveal an uplift pattern that decreases with greater
494 distances from the fault along the footwall (Fig. 4A-D). The recorded wavelength correlates with
495 the thickness of the brittle faulted layer constrained by the maximum depth of recorded
496 earthquakes (Olive et al., 2022; Table S2; Figs. 4A1-A4) where the Paeroa Range (Fig. 4A1) exhibits
497 the narrowest uplift wavelength followed by the Sandia (Fig. 4A2), Wassuk (Fig. 4A3), and
498 Kipengere (Fig. 4A4) ranges.

499 For the Sandia Mountains, inversions assuming both uniform and variable erodibility yield
500 nearly identical uplift wavelengths. However, the former yields an unrealistic peak in the uplift
501 field 8 km from the fault (Fig. 4A2), which could be an artifact of spatially-variable erodibility. An
502 inversion that accounts for a different erodibility in the Western and Eastern sides of the range
503 indeed yields a more straightforward uplift field that continuously decays with distance to the
504 fault. It also produces less scatter in χ values (Fig. 4B2) and determines that Sandia granite (West
505 side) is 2.2 times more erodible than the Madera formation limestone (East side, Fig. 4C2). This
506 is consistent with the notion that high infiltration rates over carbonate landscapes deprive rivers
507 from water and therefore erosive power, while much greater surface runoff enhances granite
508 denudation. This result underscores the importance of considering variable erodibility when
509 inferring tectonic uplift fields.

510 We highlight that our inversion method is designed to recover the coefficients controlling the B-
511 spline knots (see Figs. S12-S15 for the posterior distributions of all inverted parameters) , which
512 can be used to describe uplift not only along the rivers utilized in the inversion but also across all
513 catchments feeding those rivers (see section 3.5.1). While this capability is clearly demonstrated

514 in the 1D inversion cases (Figs. 4C1-4), its true strength lies in capturing complex spatial attributes
515 across two dimensions. For example, our 2-D inversion for the Lemhi landscape effectively
516 captures the spatial variations in uplift expected near the tip of a normal fault within the Lemhi
517 Range. It shows diminishing uplift within 10 km to the fault tip (Fig. 4A5), aligning with previously
518 documented k_{sn} values in the region (Densmore et al., 2007), and a general decrease in uplift
519 with increasing distance from the fault axis (Fig. 4C5). These observations demonstrate our
520 model's ability to accurately infer two-dimensional variations in uplift.

521 Similar to our synthetic landscapes (Figs. 2C, S2-5), inverting for uplift patterns yields RMS
522 values that are 2-3 times better than those assuming a uniform uplift pattern. This is visually
523 supported by the tight alignment of χ values around the recovered a_s particularly in the Wassuk
524 range case where χ values that do not account for uplift gradients form three distinct branches
525 in contrast to the neatly aligned χ values for the inversion that accounts for uplift variations (Fig.
526 4B3). Additionally, the average recovered m/n ratio is closer to $\theta = 0.45$, a value considered
527 typical for natural landscapes (Gailleton et al., 2021; Mudd et al., 2014; Snyder et al., 2000). The
528 Wassuk Range shows relatively large deviation with an m/n ratio of 0.22. However, when we
529 invert the landscape while fixing $n=1$ and $m=0.45$ we recover an uplift pattern that closely
530 resembles the original with an RMS value larger by 1.4 (Fig. S16).

531 We note that the Malawi landscape exhibits the highest RMS value compared to other
532 landscapes shaped by normal faults (Fig. 4). The steep, incised topography of the Kipengere Ridge
533 indicates strong fluvial incision driven by detachment-limited processes near the fault. However,
534 fluvial incision driven by the Livingstone fault system extend into smoother, sediment-filled
535 valleys about 40 km away, where hillslope diffusion and sediment deposition contribute to
536 elevation misfits. These contrasting landscape features likely explain the larger misfits in Malawi
537 compared to other landscapes with smaller RMS values.

538

539 5.3.2 The Himalayas

540

541 Our inversion results for the Himalayan section reveal a distinct region of uplift
542 approximately 100 km N-NE of the main frontal thrust, extending from the eastern to the western

543 end of the study area (Fig. 5A). This finding aligns well with previous estimates (Fig. 5G) derived
544 from fluvial incision rates observed in terraces, channel geometry (Lavé & Avouac, 2001), ^{10}Be
545 concentrations in detrital sediments (Godard et al., 2014), 1-D river profile analysis (Meade,
546 2010) and k_{sn} values (Clubb et al., 2023). Additionally, we identify a second uplift peak closer to
547 the frontal thrust on the southwestern end. The uncertainty associated with this peak is larger
548 (Fig. 5C) due to the sparse river network in the region, which limits the constraints on the B-spline
549 coefficients and reduces our confidence in interpreting this feature.

550 In contrast to the Sandia Mountains (Fig. 4A2), where erodibility values exhibited
551 significant contrast and strongly influenced the inverted uplift patterns, the recovered erodibility
552 values in the Himalayas (e.g., Fig. 5D) are relatively uniform, with values within one standard
553 deviation of each other (Table S3). This suggests that spatial variations in erodibility does not play
554 a major role in shaping the landscape in this section of the Himalayas.

555 To assess the influence of climate patterns, we performed an additional inversion that
556 excluded the effects of variable precipitation. Although this inversion resulted in RMS values that
557 were higher by a factor of 1.3 (Fig. 5B), it revealed similar overall features, including an uplift
558 peak extending from east to west (Fig. 5F), indicating that the impact of climate on this section
559 of the Himalayas may be negligible (e.g., Godard et al., 2014).

560 6 Discussion

561 6.1 Applicability and limits of the methods: Insights from synthetic landscapes

562

563 By examining synthetic landscapes we show that pronounced hillslope diffusion and
564 sediment transport lead to reduced accuracy of recovered landscape properties. Significant
565 sedimentation in mountain ranges depart from the detachment-limited models we use, leading
566 to discrepancy between inverted and imposed uplift (Fig. 3B1). Satellite imagery offers a reliable
567 method to identify regions with pronounced sediment cover, allowing us to focus on basins with
568 predominantly bedrock rivers (e.g., Perron & Royden, 2013; Wobus et al., 2006).

569 The impact of hillslope diffusion is more uniform across the landscape and thus more
570 challenging to circumvent. However, our synthetic landscape analyses suggest that only in case

571 of exceptionally pronounced hillslope diffusion do our recovered uplift patterns starkly diverge
572 from the imposed uplift (see Litwin et al., in rev. for a corrective solution). Such high values of
573 hillslope diffusion should form natural landscapes with smooth features that are easy to identify
574 and avoid (e.g., Fig. 3B2). We note that our synthetic hillslope diffusion model does not account
575 for changes in diffusion rates across landscapes (e.g., Auzet & Ambroise, 1996; Bontemps et al.,
576 2020; Matsuoka, 1998). Additionally, our underlying assumption is that channel width is a power-
577 law function of discharge manifested as a change in the effective exponent m . In reality, however,
578 river channels width may vary locally, with narrower channels increasing erosion (Lavé & Avouac,
579 2001; Yanites et al., 2010), which in our case would likely result in unrealistic high inverted uplift
580 pattern.

581 Our study of synthetic landscapes adjusting to a change in uplift rates and patterns reveals
582 that if more than half the required time to reach a new equilibrium has passed, our inversion
583 accurately recovers the uplift signal (Fig. 3A5). In our simulations, temporal changes are modeled
584 as instantaneous steps while in natural settings, these variations may unfold over extended
585 periods. For example, Smith et al. (2024) used river profiles along the normal fault-bound
586 Wasatch Range, demonstrating that uplift rates fluctuate temporally up to threefold within as
587 little as 400 ky suggesting that the landscape may never achieve quasi steady state. Similarly,
588 when we model changes in uplift rates over comparable durations, our inversion method
589 successfully recovers uplift patterns closely resembling the imposed ones (Text S3; Fig. S17),
590 despite the landscapes being far from steady state. This echoes our findings from instantaneous
591 step changes experiment (Fig. 3A5), confirming that even when landscapes are not in steady
592 state, our inversion can retrieve uplift patterns that mirror the imposed ones. This indicates that
593 when we apply our inversion to natural landscapes, we likely extract a value of a_s that reflects a
594 time-averaged window and an uplift pattern that shows minor deviation from the time-averaged
595 tectonic uplift. This is partly because working in the χ framework lets us treat the river network
596 as a cohesive system, integrating the contributions of all river nodes, as opposed to local
597 approaches such as k_{sn} .

598 In contrast, temporal variations in spatial uplift pattern are typically slower and less
599 frequent. Adjustments in fault orientation or dip angle, which can alter uplift patterns, are either

600 slow and progressive (e.g., Olive & Behn, 2014; Oryan & Buck, 2020) or result in the formation of
601 new faults rather than modifying existing ones (e.g., Taylor & Switzer, 2001). These new faults
602 should form far enough from the original faults and may not significantly impact the associated
603 uplift pattern. Our synthetic landscape experiments exploring the effects of gradual temporal
604 changes in uplift patterns demonstrate that, as long as the imposed changes are slow enough,
605 our method accurately extracts uplift patterns that closely resemble the original ones (Text S4;
606 Fig. S18).

607 Our synthetic landscape analyses also demonstrate that spatial variations in erodibility and
608 precipitation can significantly alter the recovered uplift pattern with discrepancy amounting to
609 RMS values of 10⁻⁵ times the original signal (Fig. 3A4). Nevertheless, we demonstrate that the
610 inversion is capable of accounting for those. This is crucial as current methods to extract uplift
611 patterns from landscapes often rely on k_{sn} (e.g., Castillo et al., 2014; Densmore et al., 2007;
612 Ponza et al., 2010; Su et al., 2017) which cannot directly distinguish between erodibility and uplift
613 given spatial varying erodibility. Our method offers a way to discern the two provided that we
614 can predefine regions with different erodibility levels based on lithological maps.

615

616 6.2 Performance on natural landscapes

617

618 Our analysis of natural landscapes further highlights the effectiveness of our inversion
619 method. For landscapes shaped by normal faults, we demonstrate that the decay length of the
620 uplift field away from the fault is directly linked to the thickness of the brittle upper crust (Figs.
621 4A1-4), consistent with standard models of normal fault-induced flexure, where a thicker elastic
622 layer typically produces a broader uplift profile (e.g., Goren et al., 2014; Nadai, 1963; Weissel &
623 Karner, 1989). We show that our method can robustly extract this signal, even when it is
624 interwoven with spatial variations in erodibility (Fig. 4A2). Additionally, we retrieve smaller uplift
625 rates around the southern Lemhi fault tip (Fig. 4A5), aligning with previous uplift estimates
626 (Densmore et al., 2007) and the notion that slip vanishes over a short distance near fault tips
627 (Ellis & Barnes, 2015; Roberts & Michetti, 2004). Our analysis of the Himalayan landscape (Fig. 5)
628 further demonstrate the success of our method in retrieving realistic uplift patterns while

629 accounting for climatic variations, showing strong alignment with previous estimates based on
630 geomorphological markers (Fig. 5G). This consistency across different tectonic settings
631 underscores the robustness of our inversion approach in accurately recovering uplift patterns
632 from natural landscapes.

633 That said, pinpointing which aspects of the retrieved signal are tied to temporal changes
634 presents an intriguing challenge. Fortunately, the Himalayas have been widely studied and offer
635 a wealth of geomorphological markers that measure uplift and denudation rates across various
636 timescales, enabling us to qualitatively assess whether the landscape is in a quasi-steady state.
637 These markers include rock-uplift rate estimates from river-profile analyses (Lavé & Avouac,
638 2001), ^{10}Be concentrations in fluvial sediments (Godard et al., 2014), apatite fission-track
639 cooling ages (Robert et al., 2009) and thermochronological data (Herman et al., 2010), capturing
640 processes operating over time scales ranging from thousands to millions of years. These
641 geomorphological markers consistently indicate a peak in uplift rate at approximately 100 km
642 from the main frontal thrust (Fig. 5G). This alignment of spatial patterns across different temporal
643 scales underscores the persistence of tectonic signals and suggests that at least our section of
644 the Himalayan landscape may be approaching a steady state.

645 Unfortunately, the landscapes shaped by normal faults used in our analysis have not been
646 extensively studied, and we are unaware of denudation rates measurements. However, as
647 mentioned above our analysis of synthetic landscapes demonstrates that we can recover uplift
648 patterns closely matching the imposed ones (Fig. 2B5), even when the landscape experiences a
649 fivefold fluctuation in uplift rate over as little as 400 kyr (Text S3; Figs. S17). Natural variations in
650 tectonic uplift, which could skew recovered uplift patterns, are likely slow enough to significantly
651 biasing our inverted uplift pattern (Section 6.1; Text S5; Fig. S19; Table S2). Additionally, most
652 landscapes have likely had sufficient time for the signal associated with fault formation to reach
653 a steady state (Text S5; Fig. S19; Table S2), indicating that our recovered uplift patterns likely
654 reflect current trends. We may overestimate or underestimate our values of a_s , but translating
655 these into absolute uplift rates is challenging and requires precise knowledge of k_0 and A_0 , two
656 parameters that are difficult to constrain accurately.

657

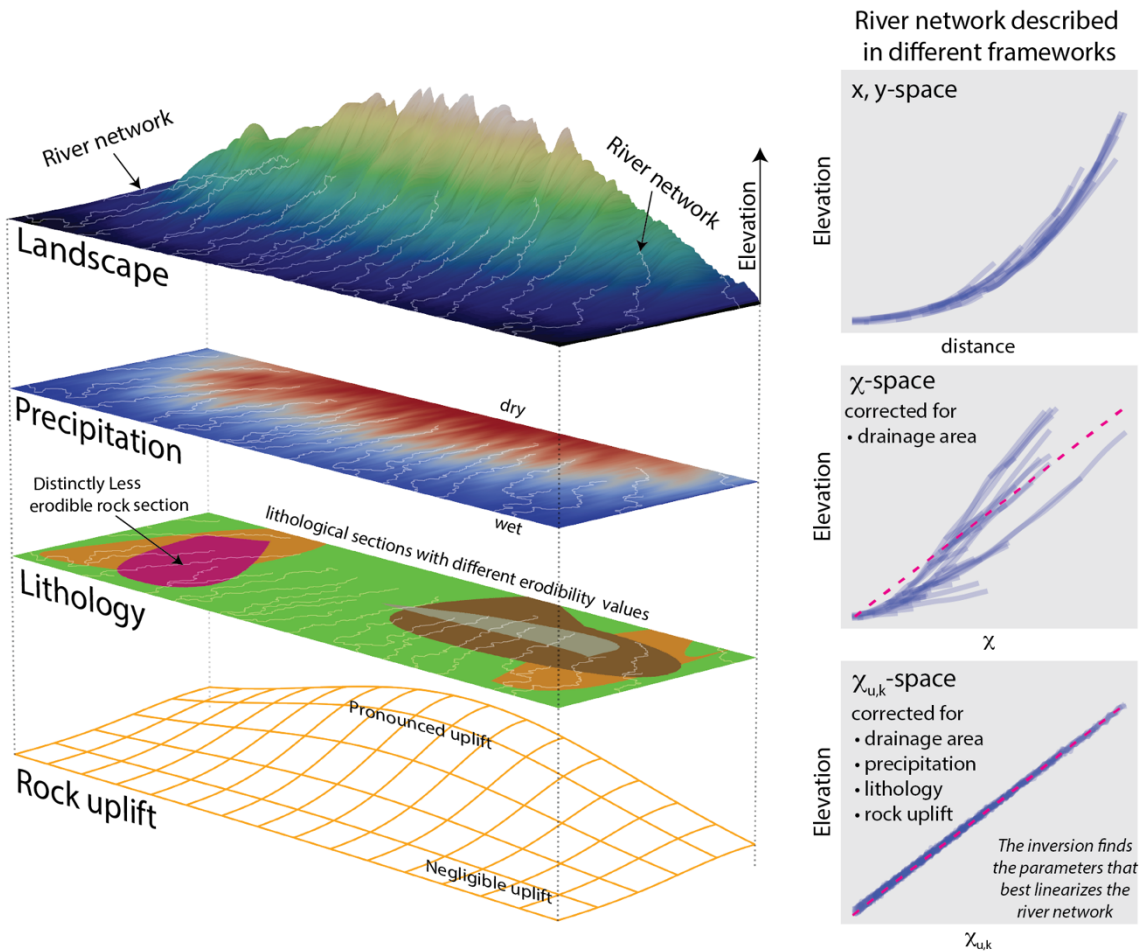
658 6.3 Future applications of our method

659

660 The success of our method in recovering uplift patterns while discerning climatic,
661 lithological and tectonic drivers in synthetic and natural landscapes suggests that it could be
662 applied to other tectonic settings where knowledge of long-term uplift rates is limited.

663 One exciting application of our method is its ability to untangle climatic and tectonic signals,
664 shedding light on the long-standing question of the relative roles of climate and tectonic forcing
665 in the evolution of orogenic regions such as the Andes and Himalayas (e.g., Leonard et al., 2023;
666 Montgomery et al., 2001; Whipple, 2009; Molnar & England, 1990). A second use of our method
667 is its ability to recover long-term uplift trends to help constrain seismic hazards along subduction
668 zones, which produce the most destructive earthquakes on Earth. Recent evidence demonstrate
669 that geodetically locked areas of subduction megathrusts (e.g., Lindsey et al., 2018; Oryan et al.,
670 2023; Steckler et al., 2016), which produce short-term interseismic surface uplift systematically
671 correlations with long-term uplift patterns shaped over thousands of years (Jolivet et al., 2020;
672 Madella & Ehlers, 2021; Malatesta et al., 2021; Meade, 2010; Saillard et al., 2017). This
673 correlation is observed in the Himalayan section we studied (Fig. 5G; Godard et al., 2014; Jackson
674 & Bilham, 1994; Lavé & Avouac, 2001; Sreejith et al., 2018) as well as in Cascadia and Chile
675 subduction zones and is attributed to the accumulation of irreversible strain during the
676 interseismic period, generating a spatially variable, permanent uplift field recorded by the
677 landscape over many seismic cycles (Oryan et al., 2024). Our inversion method opens the door
678 to leveraging these time-averaged signals captured in landscapes over tens of thousands of years
679 and hundreds of earthquake cycles, offering valuable insights into persistent plate coupling and
680 the associated seismic hazards over extended timescales.

681

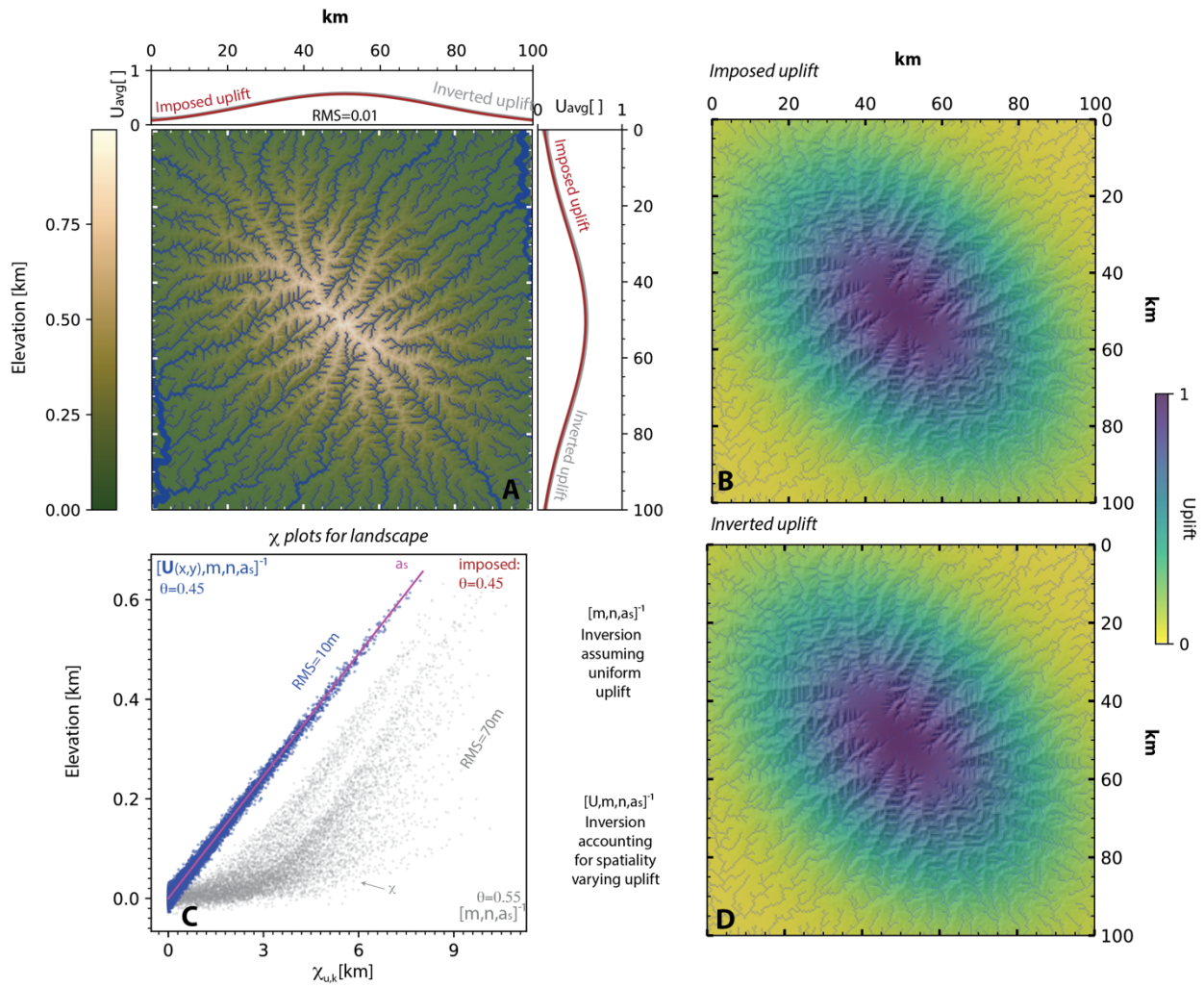


683

684 Figure 1 – **Illustration of a fluvially-incised landscape and its river networks.** Left: Panels depict
 685 the tectonic, lithological, and climatic factors shaping the landscape. Right: The river network
 686 incising the landscape is described using three geomorphological frameworks, with the lower
 687 panel showing the framework used in our approach.

688

Inversion of detachment limit synthetic landscape

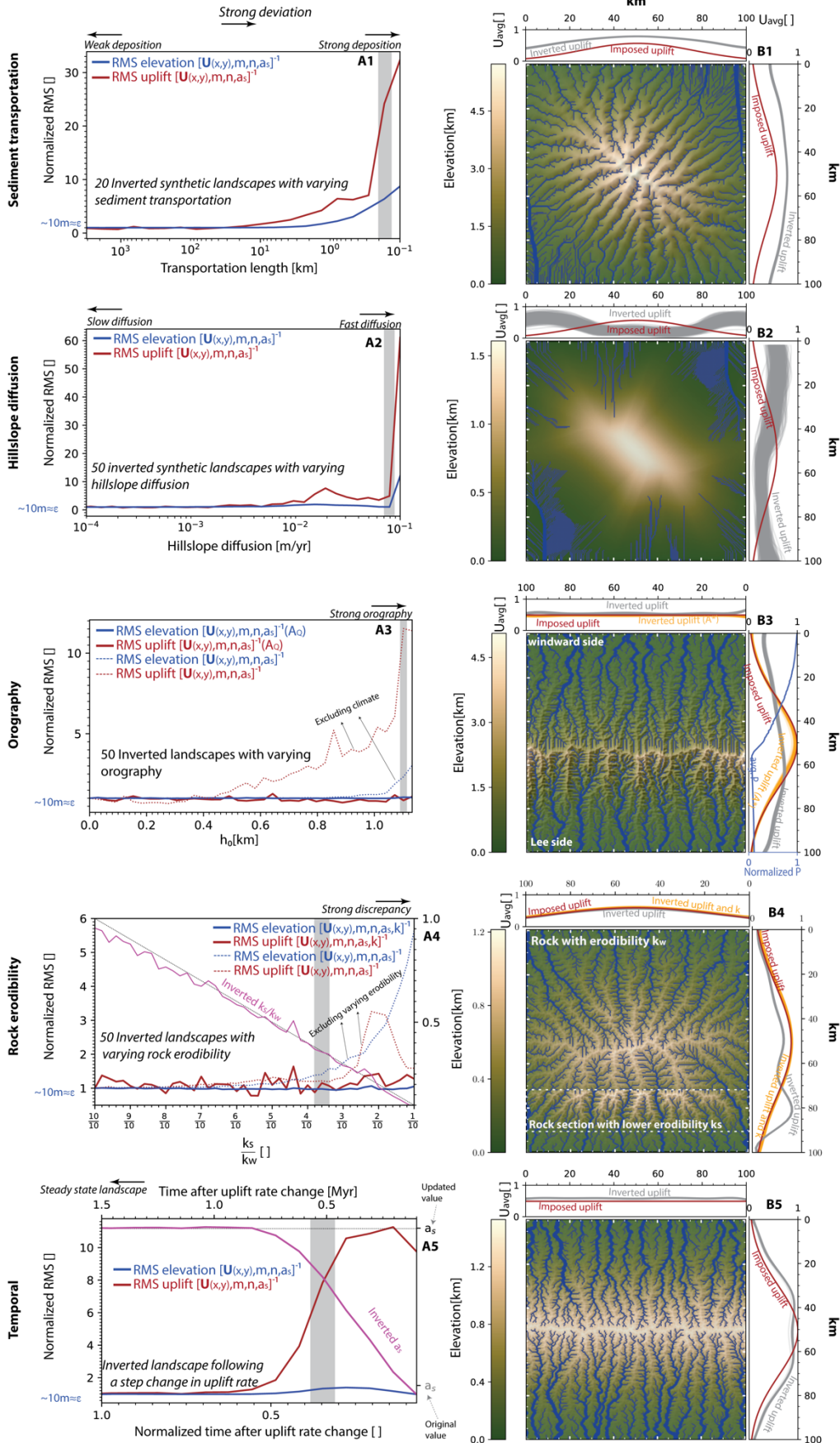


689

690 **Figure 2 – Inverted detachment limited synthetic landscape.** A – Landscape terrain. Blue dots
 691 show 8000 river nodes used to constrain the inversion with dot size proportional to the drainage
 692 area. Marginal plots show average uplift along axis. Imposed uplift is shown in red curve and 500
 693 samples randomly drawn from the inverted uplift posterior distribution and extrapolated to the
 694 domain are shown in grey. B – Imposed uplift function used during the simulation of the
 695 landscape. Dots show river nodes used in the inversion. C – Points show measured elevation
 696 (z_{obs}) for 8000 river nodes and χ values derived from best inverted solution. Blue and grey
 697 denote inversion results including and excluding uplift, respectively. D – Best inverted uplift
 698 solution extrapolated for the entire domain. Dots mark river nodes used to constrain the
 699 inversion.

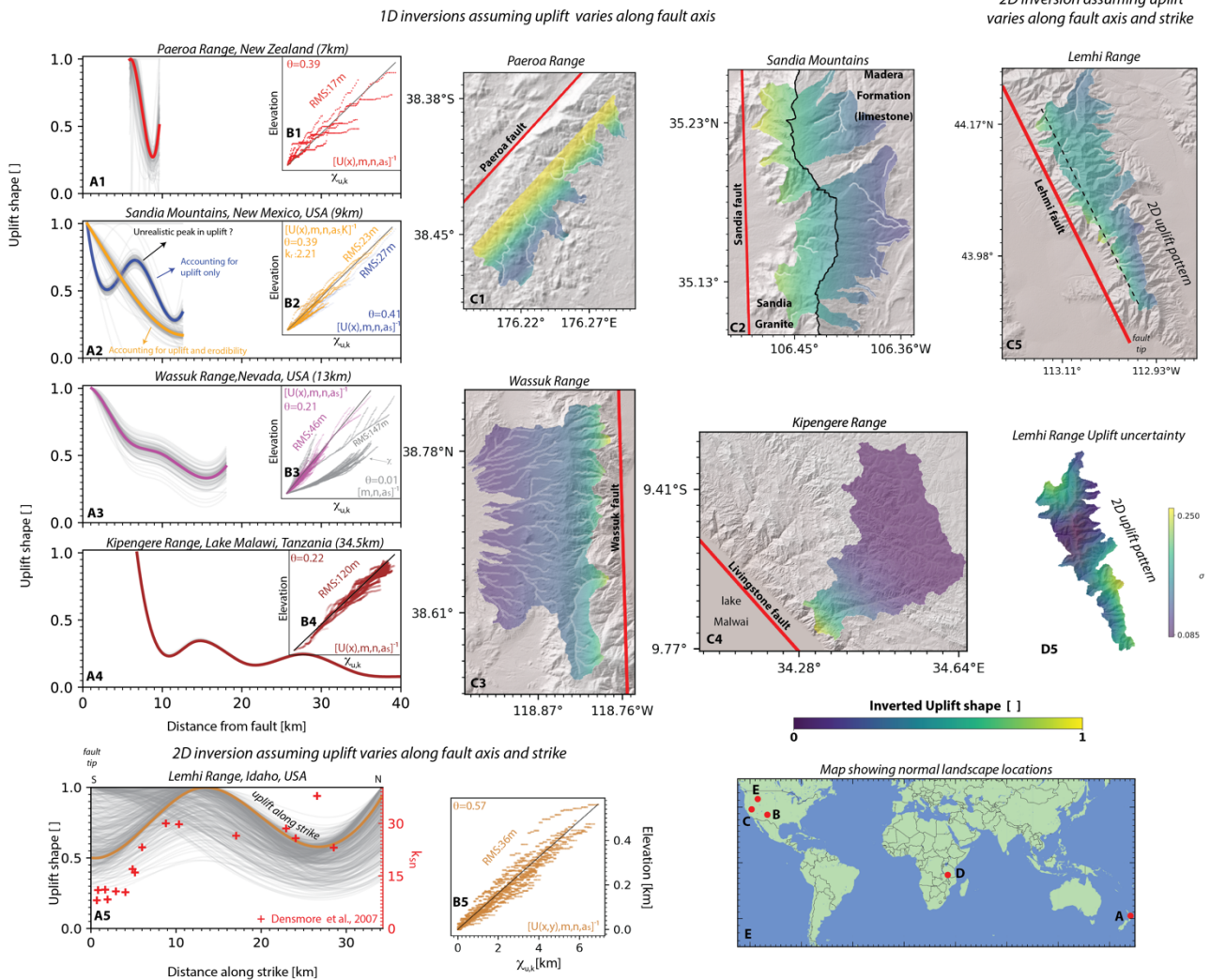
700

Inversion of synthetic landscapes deviating from detachment limited model



702 **Figure 3 – Inverted synthetic landscapes deviating from the detachment limited model showing**
703 **varying degrees of hillslope diffusion (1), sediment deposition(2), orographic effects(3), spatial**
704 **variations in erodibility(4), and temporal changes in uplift rates(5).** A - RMS values for elevation
705 and uplift and normalized with respect to value obtained for the detachment limited landscape
706 (Fig 1). ε denote error we introduced amounting to 10m (See section 4.2). Grey vertical line shows
707 an example landscape described in panel B. B -Landscape Elevation. Blue dots show 8000 river
708 nodes used for the inversion with dot size proportional to the drainage area. Marginal plots show
709 average uplift along axis. Imposed uplift is shown in red curve and 500 samples randomly drawn
710 from the inverted uplift posterior distribution and extrapolated to the domain are shown in grey
711 and orange colors. Panels A4 and A5 show the inverted and imposed parameters k_w/k_s and a_s
712 in magenta and dashed black line, respectively. The x-axis in Panel A5 displays time in million
713 years (top) and as a fraction of the time it takes for the landscape to reach steady state(bottom).
714
715
716
717
718
719
720
721
722
723
724
725
726

Inverted landscapes shaped by normal faults

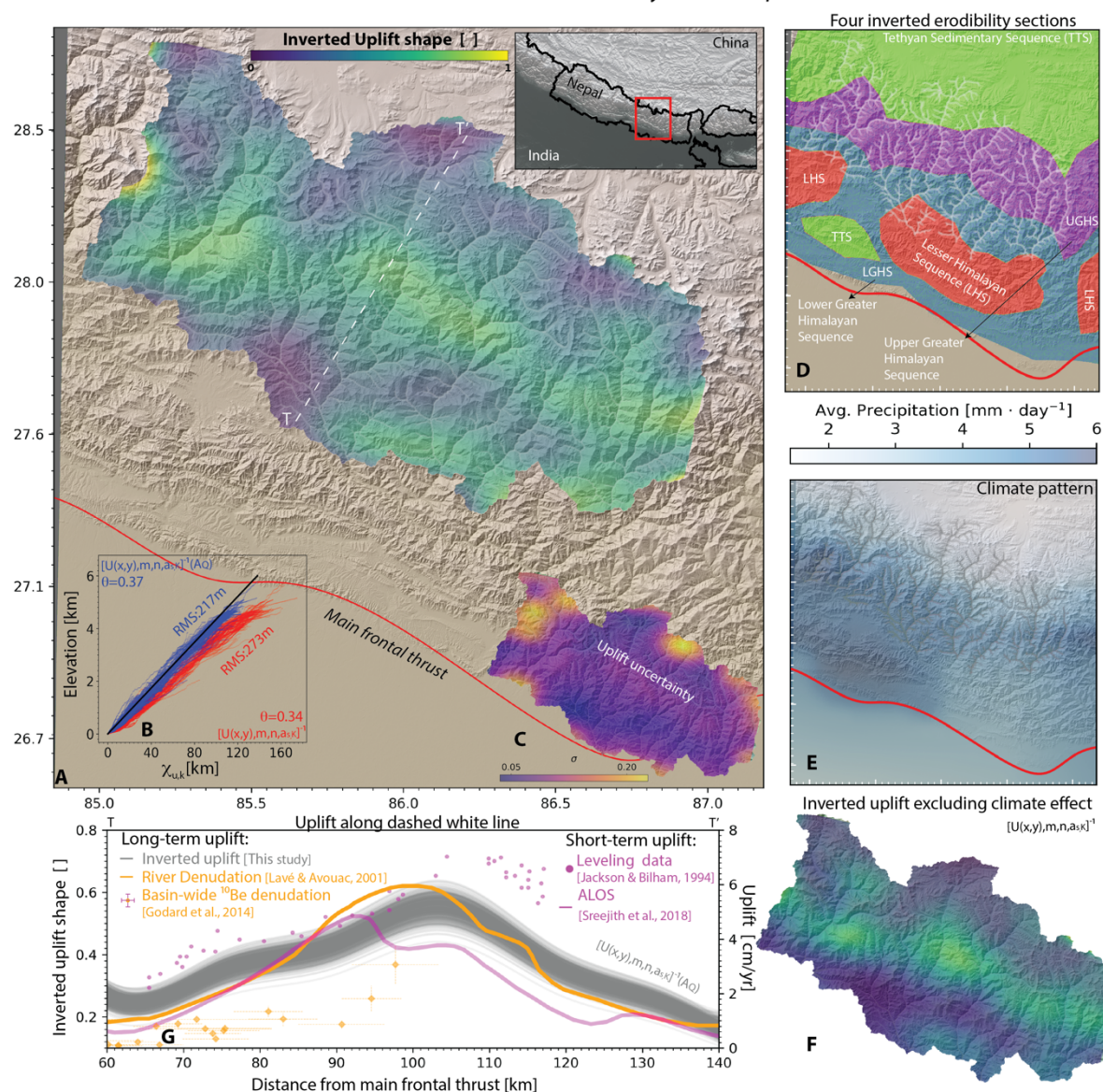


727
 728
 729
 730
 731
 732
 733
 734
 735
 736
 737
 738
 739
 740
 741
 742

Figure 4 – 1D (1-4) and 2D (5) inversions of five natural landscapes shaped by normal faults. A – Best-fitting uplift pattern as a function of distance from the fault is represented by colored curves, with 500 uplift solutions randomly sampled from the posterior distribution shown as grey lines. In A5, the uplift is displayed along strike, following the dashed black line shown in C5. Red markers indicate k_{sn} values computed by Densmore et al. (2007). B - Colored dots represent the χ values for the best-fitting solution for river nodes used in the inversion. Black line marks the inverted slope a_s . Elevation indicates the relief from the base level. The parameter θ denotes the ratio of the inverted m/n values. In A2, k_r shows the erodibility ratio for two inverted rock sections in Sandia. C - The uplift pattern is displayed within the catchments feeding the rivers used in the inversion, highlighted in light white. The fault position is indicated by a red line. In C2, the positions of two lithological sections are shown to the right and left of the ridge line, which is marked by a black line. D – Uplift standard deviation, represented by the colormap, is calculated

743 by evaluating the uplift at each pixel using 500 samples randomly drawn from the posterior
744 distribution. E – map showing landscapes locations.
745

Inverted Himalaya landscape



746
 747 **Figure 5 – Inversion results for Himalaya landscape.** A – Best-fitting uplift pattern for the
 748 inversion including climate effect is displayed within the catchments feeding the rivers used in
 749 the inversion, highlighted by light white dots. White dashed line shows the profile used to plot
 750 uplift in panel F. B - Colored dots represent the χ values for the best-fitting solution for river nodes
 751 used in the inversion including (blue) and excluding (red) climate effects. Black line marks the
 752 best fitting inverted slope a_s . Elevation indicates the relief from the base level. The parameter θ
 753 denotes the ratio of the inverted m/n values. C- Uplift standard deviation is calculated by
 754 evaluating the uplift at each pixel using 500 samples randomly drawn from the posterior
 755 distribution. D – Four distinct lithological sections (Carosi et al., 2018) used to constrain the
 756 spatial variability of four inverted erodibility values. River nodes used in the inversion are marked
 757 by white dots. E – Average climate pattern used to constrain the climate drainage area, A_Q
 758 (section 3.1.4). River nodes used in the inversion are shown by gray dots. F – best fitting uplift

759 pattern for the inversion excluding climate effects. G– Gray curves represent 500 uplift patterns
760 randomly drawn from the posterior distribution along a line perpendicular to the main frontal
761 thrust. Long-term (Godard et al., 2014; Lavé & Avouac, 2001) rates and short-term (Jackson &
762 Bilham, 1994; Sreejith et al., 2018) uplift recorded during the interseismic period are indicated
763 by orange and magenta colors, respectively.
764

765

766 8 Funding

767

768 This work was funded by the Emergence(s)–Ville de Paris Program Project “Inelasticity in the
769 Subduction earthquake cycle” (J.-A.O.); the French Agence Nationale de la Recherche (ANR) grant
770 GeoSigMA (J.-A.O.), the European Research Council (ERC) under the European Union’s horizon
771 2020 research and innovation program, Geo-4d project, grant agreement 758210 (R.J.); institut
772 Universitaire de France (R.J.); h2020 european Research council, grant no. 803721 (B.G.);
773 Chateaubriand Fellowship Program ,Green Postdoctoral Scholarship from IGPP at SIO and
774 national Science Foundation, grant no. nSF-OAc- 2311208 (B.O.)

775

776 9 Open Research

777

778 The Digital Elevation Models (DEMs) utilized in this study were sourced from the Shuttle Radar
779 Topography Mission (Farr et al., 2007) and are freely available at
780 <https://www.opentopography.org/>. Precipitation data were obtained from the NASA Global
781 Precipitation Measurement mission (Huffman et al., 2015), accessible at
782 <https://gpm.nasa.gov/data>. The specific DEM, precipitation data, and code used for the inversion
783 in this paper are freely accessible at <https://zenodo.org/records/14029506>. Synthetic landscapes
784 were generated using CHONK (Gailleton et al., 2024). Figures were produced using GMT (Wessel
785 et al., 2019), Matplotlib (Caswell et al., 2021) and Adobe Illustrator
786 (<https://www.adobe.com/products/illustrator.html>).

787

788 10 References

- 789 Akaike, H. (1974). A new look at the statistical model identification. *IEEE Transactions on*
790 *Automatic Control*, 19(6), 716–723. <https://doi.org/10.1109/TAC.1974.1100705>
- 791 Anderson, J. L. (2007). An adaptive covariance inflation error correction algorithm for ensemble
792 filters. *Tellus A: Dynamic Meteorology and Oceanography*, 59(2), 210.
793 <https://doi.org/10.1111/j.1600-0870.2006.00216.x>
- 794 Armijo, R., Meyer, B., King, G. C. P., Rigo, A., & Papanastassiou, D. (1996). Quaternary evolution
795 of the Corinth Rift and its implications for the Late Cenozoic evolution of the Aegean.
796 *Geophysical Journal International*, 126(1), 11–53. [https://doi.org/10.1111/j.1365-](https://doi.org/10.1111/j.1365-246X.1996.tb05264.x)
797 [246X.1996.tb05264.x](https://doi.org/10.1111/j.1365-246X.1996.tb05264.x)
- 798 Auzet, A.-V., & Ambroise, B. (1996). Soil Creep Dynamics, Soil Moisture and Temperature
799 Conditions on a Forested Slope in the Granitic Vosges Mountains, France. *Earth Surface*
800 *Processes and Landforms*, 21(6), 531–542. [https://doi.org/10.1002/\(SICI\)1096-](https://doi.org/10.1002/(SICI)1096-9837(199606)21:6<531::AID-ESP606>3.0.CO;2-B)
801 [9837\(199606\)21:6<531::AID-ESP606>3.0.CO;2-B](https://doi.org/10.1002/(SICI)1096-9837(199606)21:6<531::AID-ESP606>3.0.CO;2-B)
- 802 Babault, J., Viaplana-Muzas, M., Legrand, X., Van Den Driessche, J., González-Quijano, M., &
803 Mudd, S. M. (2018). Source-to-sink constraints on tectonic and sedimentary evolution of
804 the western Central Range and Cenderawasih Bay (Indonesia). *Journal of Asian Earth*
805 *Sciences*, 156, 265–287. <https://doi.org/10.1016/j.jseaes.2018.02.004>
- 806 Bishop, C. M. (2006). *Pattern recognition and machine learning* (Vol. 4). Springer. Retrieved from
807 <https://link.springer.com/book/9780387310732>

808 Bontemps, N., Lacroix, P., Larose, E., Jara, J., & Taïpe, E. (2020). Rain and small earthquakes
809 maintain a slow-moving landslide in a persistent critical state. *Nature Communications*,
810 11(1), 780. <https://doi.org/10.1038/s41467-020-14445-3>

811 Bookhagen, B., & Burbank, D. W. (2010). Toward a complete Himalayan hydrological budget:
812 Spatiotemporal distribution of snowmelt and rainfall and their impact on river discharge.
813 *Journal of Geophysical Research: Earth Surface*, 115(F3).
814 <https://doi.org/10.1029/2009JF001426>

815 Campforts, B., Vanacker, V., Herman, F., Vanmaercke, M., Schwanghart, W., Tenorio, G. E., et al.
816 (2020). Parameterization of river incision models requires accounting for environmental
817 heterogeneity: insights from the tropical Andes. *Earth Surface Dynamics*, 8(2), 447–470.
818 <https://doi.org/10.5194/esurf-8-447-2020>

819 Carosi, R., Montomoli, C., & Iaccarino, S. (2018). 20 years of geological mapping of the
820 metamorphic core across Central and Eastern Himalayas. *Earth-Science Reviews*, 177,
821 124–138. <https://doi.org/10.1016/j.earscirev.2017.11.006>

822 Carretier, S., Martinod, P., Reich, M., & Godderis, Y. (2016). Modelling sediment clasts transport
823 during landscape evolution. *Earth Surface Dynamics*, 4(1), 237–251.
824 <https://doi.org/10.5194/esurf-4-237-2016>

825 Castillo, M., Muñoz-Salinas, E., & Ferrari, L. (2014). Response of a landscape to tectonics using
826 channel steepness indices (*k_{sn}*) and OSL: A case of study from the Jalisco Block, Western
827 Mexico. *Geomorphology*, 221, 204–214.
828 <https://doi.org/10.1016/j.geomorph.2014.06.017>

829 Caswell, T. A., Droettboom, M., Lee, A., Andrade, E. S. de, Hoffmann, T., Hunter, J., et al. (2021,
830 August 13). matplotlib/matplotlib: REL: v3.4.3. Zenodo.
831 <https://doi.org/10.5281/zenodo.5194481>

832 Cattin, R., & Avouac, J. P. (2000). Modeling mountain building and the seismic cycle in the
833 Himalaya of Nepal. *Journal of Geophysical Research: Solid Earth*, *105*(B6), 13389–13407.
834 <https://doi.org/10.1029/2000JB900032>

835 Clubb, F. J., Mudd, S. M., Schildgen, T. F., van der Beek, P. A., Devrani, R., & Sinclair, H. D. (2023).
836 Himalayan valley-floor widths controlled by tectonically driven exhumation. *Nature*
837 *Geoscience*, *16*(8), 739–746. <https://doi.org/10.1038/s41561-023-01238-8>

838 Cordonnier, G., Bovy, B., & Braun, J. (2019). A versatile, linear complexity algorithm for flow
839 routing in topographies with depressions. *Earth Surface Dynamics*, *7*(2), 549–562.
840 <https://doi.org/10.5194/esurf-7-549-2019>

841 Croissant, T., & Braun, J. (2014). Constraining the stream power law: a novel approach combining
842 a landscape evolution model and an inversion method. *Earth Surface Dynamics*, *2*(1),
843 155–166. <https://doi.org/10.5194/esurf-2-155-2014>

844 Dal Zilio, L., Hetényi, G., Hubbard, J., & Bollinger, L. (2021). Building the Himalaya from tectonic
845 to earthquake scales. *Nature Reviews Earth & Environment*, *2*(4), 251–268.
846 <https://doi.org/10.1038/s43017-021-00143-1>

847 Davy, P., & Lague, D. (2009). Fluvial erosion/transport equation of landscape evolution models
848 revisited. *Journal of Geophysical Research: Earth Surface*, *114*(F3).
849 <https://doi.org/10.1029/2008JF001146>

850 Densmore, A. L., Gupta, S., Allen, P. A., & Dawers, N. H. (2007). Transient landscapes at fault tips.
851 *Journal of Geophysical Research*, 112(F3), F03S08.
852 <https://doi.org/10.1029/2006JF000560>

853 Dublanchet, P., & Olive, J.-A. (2024). Inelastic deformation accrued over multiple seismic cycles:
854 Insights from an elastic-plastic slider-and-springboard model. *Seismica*, 3(2).
855 <https://doi.org/10.26443/seismica.v3i2.1345>

856 Ellis, M. A., & Barnes, J. B. (2015). A global perspective on the topographic response to fault
857 growth. *Geosphere*, 11(4), 1008–1023. <https://doi.org/10.1130/GES01156.1>

858 Faccenna, C., Glišović, P., Forte, A., Becker, T. W., Garzanti, E., Sembroni, A., & Gvirtzman, Z.
859 (2019). Role of dynamic topography in sustaining the Nile River over 30 million years.
860 *Nature Geoscience*, 12(12), 1012–1017. <https://doi.org/10.1038/s41561-019-0472-x>

861 Farr, T. G., Rosen, P. A., Caro, E., Crippen, R., Duren, R., Hensley, S., et al. (2007). The Shuttle
862 Radar Topography Mission. *Reviews of Geophysics*, 45(2).
863 <https://doi.org/10.1029/2005RG000183>

864 Fox, M., Goren, L., May, D. A., & Willett, S. D. (2014). Inversion of fluvial channels for paleorock
865 uplift rates in Taiwan. *Journal of Geophysical Research: Earth Surface*, 119(9), 1853–1875.
866 <https://doi.org/10.1002/2014JF003196>

867 Gailleton, B., Sinclair, H. D., Mudd, S. M., Graf, E. L. S., & Mañenco, L. C. (2021). Isolating Lithologic
868 Versus Tectonic Signals of River Profiles to Test Orogenic Models for the Eastern and
869 Southeastern Carpathians. *Journal of Geophysical Research: Earth Surface*, 126(8),
870 e2020JF005970. <https://doi.org/10.1029/2020JF005970>

871 Gailleton, Boris, Mudd, S. M., Clubb, F. J., Grieve, S. W. D., & Hurst, M. D. (2021). Impact of
872 Changing Concavity Indices on Channel Steepness and Divide Migration Metrics. *Journal*
873 *of Geophysical Research: Earth Surface*, 126(10), e2020JF006060.
874 <https://doi.org/10.1029/2020JF006060>

875 Gailleton, Boris, Malatesta, L. C., Cordonnier, G., & Braun, J. (2024). CHONK 1.0: landscape
876 evolution framework: cellular automata meets graph theory. *Geoscientific Model*
877 *Development*, 17(1), 71–90. <https://doi.org/10.5194/gmd-17-71-2024>

878 Godard, V., Bourles, D. L., Spinabella, F., Burbank, D. W., Bookhagen, B., Fisher, G. B., et al. (2014).
879 Dominance of tectonics over climate in Himalayan denudation. *Geology*, 42(3), 243–246.
880 <https://doi.org/10.1130/G35342.1>

881 Goren, L., Fox, M., & Willett, S. D. (2014). Tectonics from fluvial topography using formal linear
882 inversion: Theory and applications to the Inyo Mountains, California. *Journal of*
883 *Geophysical Research: Earth Surface*, 119(8), 1651–1681.
884 <https://doi.org/10.1002/2014JF003079>

885 Goren, Liran, Fox, M., & Willett, S. D. (2022). Linear Inversion of Fluvial Long Profiles to Infer
886 Tectonic Uplift Histories. In *Treatise on Geomorphology* (pp. 225–248). Elsevier.
887 <https://doi.org/10.1016/B978-0-12-818234-5.00075-4>

888 Hack, J. T. (1973). *Stream-profile analysis and stream-gradient index*. U.S. Geological Survey.

889 Harel, M.-A., Mudd, S. M., & Attal, M. (2016). Global analysis of the stream power law parameters
890 based on worldwide ¹⁰Be denudation rates. *Geomorphology*, 268, 184–196.
891 <https://doi.org/10.1016/j.geomorph.2016.05.035>

892 Hergarten, S., & Robl, J. (2022). The linear feedback precipitation model (LFPM 1.0) – a simple
893 and efficient model for orographic precipitation in the context of landform evolution
894 modeling. *Geoscientific Model Development*, 15(5), 2063–2084.
895 <https://doi.org/10.5194/gmd-15-2063-2022>

896 Herman, F., Copeland, P., Avouac, J.-P., Bollinger, L., Mahéo, G., Le Fort, P., et al. (2010).
897 Exhumation, crustal deformation, and thermal structure of the Nepal Himalaya derived
898 from the inversion of thermochronological and thermobarometric data and modeling of
899 the topography. *Journal of Geophysical Research: Solid Earth*, 115(B6).
900 <https://doi.org/10.1029/2008JB006126>

901 Holtmann, R., Cattin, R., Simoes, M., & Steer, P. (2023). Revealing the hidden signature of fault
902 slip history in the morphology of degrading scarps. *Scientific Reports*, 13(1), 3856.
903 <https://doi.org/10.1038/s41598-023-30772-z>

904 Howard, A. D., & Kerby, G. (1983). Channel changes in badlands. *GSA Bulletin*, 94(6), 739–752.
905 [https://doi.org/10.1130/0016-7606\(1983\)94<739:CCIB>2.0.CO;2](https://doi.org/10.1130/0016-7606(1983)94<739:CCIB>2.0.CO;2)

906 Huffman, G. J., Bolvin, D. T., Braithwaite, D., Hsu, K., Joyce, R., Xie, P., & Yoo, S.-H. (2015). NASA
907 global precipitation measurement (GPM) integrated multi-satellite retrievals for GPM
908 (IMERG). *Algorithm Theoretical Basis Document (ATBD) Version*, 4(26), 30.

909 Jackson, M., & Bilham, R. (1994). Constraints on Himalayan deformation inferred from vertical
910 velocity fields in Nepal and Tibet. *Journal of Geophysical Research: Solid Earth*, 99(B7),
911 13897–13912. <https://doi.org/10.1029/94JB00714>

912 Jolivet, R., Simons, M., Duputel, Z., Olive, J., Bhat, H. S., & Bletery, Q. (2020). Interseismic loading
913 of subduction megathrust drives long term uplift in northern Chile, 1–21.
914 <https://doi.org/10.1029/2019GL085377>

915 King, G. C. P., Stein, R. S., & Rundle, J. B. (1988). The Growth of Geological Structures by Repeated
916 Earthquakes 1. Conceptual Framework. *Journal of Geophysical Research: Solid Earth*,
917 *93*(B11), 13307–13318. <https://doi.org/10.1029/JB093iB11p13307>

918 Kirby, E., & Whipple, K. X. (2012). Expression of active tectonics in erosional landscapes. *Journal*
919 *of Structural Geology*, *44*, 54–75. <https://doi.org/10.1016/j.jsg.2012.07.009>

920 Lavé, J., & Avouac, J. P. (2001). Fluvial incision and tectonic uplift across the Himalayas of central
921 Nepal. *Journal of Geophysical Research: Solid Earth*, *106*(B11), 26561–26591.
922 <https://doi.org/10.1029/2001JB000359>

923 Leonard, J. S., & Whipple, K. X. (2021). Influence of Spatial Rainfall Gradients on River Longitudinal
924 Profiles and the Topographic Expression of Spatially and Temporally Variable Climates in
925 Mountain Landscapes. *Journal of Geophysical Research: Earth Surface*, *126*(12),
926 e2021JF006183. <https://doi.org/10.1029/2021JF006183>

927 Leonard, J. S., Whipple, K. X., & Heimsath, A. M. (2023). Isolating climatic, tectonic, and lithologic
928 controls on mountain landscape evolution. *Science Advances*, *9*(3), eadd8915.
929 <https://doi.org/10.1126/sciadv.add8915>

930 Lindsey, E. O., Almeida, R., Mallick, R., Hubbard, J., Bradley, K., Tsang, L. L. H., et al. (2018).
931 Structural Control on Downdip Locking Extent of the Himalayan Megathrust. *Journal of*
932 *Geophysical Research: Solid Earth*, *123*(6), 5265–5278.
933 <https://doi.org/10.1029/2018JB015868>

934 Madella, A., & Ehlers, T. A. (2021). Contribution of background seismicity to forearc uplift. *Nature*
935 *Geoscience*, 1–6. <https://doi.org/10.1038/s41561-021-00779-0>

936 Malatesta, L. C., Bruhat, L., Finnegan, N. J., & Olive, J.-A. L. (2021). Co-location of the Downdip
937 End of Seismic Coupling and the Continental Shelf Break. *Journal of Geophysical Research:*
938 *Solid Earth*, 126(1), e2020JB019589. <https://doi.org/10.1029/2020JB019589>

939 Matsuoka, N. (1998). The relationship between frost heave and downslope soil movement: field
940 measurements in the Japanese Alps. *Permafrost and Periglacial Processes*, 9(2), 121–133.
941 [https://doi.org/10.1002/\(SICI\)1099-1530\(199804/06\)9:2<121::AID-PPP281>3.0.CO;2-C](https://doi.org/10.1002/(SICI)1099-1530(199804/06)9:2<121::AID-PPP281>3.0.CO;2-C)

942 Meade, B. J. (2010). The signature of an unbalanced earthquake cycle in Himalayan topography?
943 *Geology*, 38(11), 987–990. <https://doi.org/10.1130/G31439.1>

944 Merritt, W. S., Letcher, R. A., & Jakeman, A. J. (2003). A review of erosion and sediment transport
945 models. *Environmental Modelling & Software*, 18(8), 761–799.
946 [https://doi.org/10.1016/S1364-8152\(03\)00078-1](https://doi.org/10.1016/S1364-8152(03)00078-1)

947 Molnar, P., & England, P. (1990). Late Cenozoic uplift of mountain ranges and global climate
948 change: chicken or egg? *Nature*, 346(6279), 29–34. <https://doi.org/10.1038/346029a0>

949 Mudd, S. M., Attal, M., Milodowski, D. T., Grieve, S. W. D., & Valters, D. A. (2014). A statistical
950 framework to quantify spatial variation in channel gradients using the integral method of
951 channel profile analysis. *Journal of Geophysical Research: Earth Surface*, 119(2), 138–152.
952 <https://doi.org/10.1002/2013JF002981>

953 Nadai, A. (1963). Theory of flow and fracture of solids. *New York, NY: McGraw-Hill*. Retrieved
954 from <https://cir.nii.ac.jp/crid/1130282270243960576>

955 O'Callaghan, J. F., & Mark, D. M. (1984). The extraction of drainage networks from digital
956 elevation data. *Computer Vision, Graphics, and Image Processing*, 28(3), 323–344.
957 [https://doi.org/10.1016/S0734-189X\(84\)80011-0](https://doi.org/10.1016/S0734-189X(84)80011-0)

958 Olive, J.-A., & Behn, M. D. (2014). Rapid rotation of normal faults due to flexural stresses: An
959 explanation for the global distribution of normal fault dips. *Journal of Geophysical*
960 *Research: Solid Earth*, 119(4), 3722–3739. <https://doi.org/10.1002/2013JB010512>

961 Olive, J.-A., Malatesta, L. C., Behn, M. D., & Buck, W. R. (2022). Sensitivity of rift tectonics to global
962 variability in the efficiency of river erosion. *Proceedings of the National Academy of*
963 *Sciences*, 119(13), e2115077119. <https://doi.org/10.1073/pnas.2115077119>

964 Oryan, B., & Buck, W. R. (2020). Larger tsunamis from megathrust earthquakes where slab dip is
965 reduced. *Nature Geoscience*. <https://doi.org/10.1038/s41561-020-0553-x>

966 Oryan, B., Betka, P. M., Steckler, M. S., Nooner, S. L., Lindsey, E. O., Mondal, D., et al. (2023). New
967 GNSS and Geological Data From the Indo-Burman Subduction Zone Indicate Active
968 Convergence on Both a Locked Megathrust and the Kabaw Fault. *Journal of Geophysical*
969 *Research: Solid Earth*, 128(4), e2022JB025550. <https://doi.org/10.1029/2022JB025550>

970 Oryan, B., Olive, J.-A., Jolivet, R., Malatesta, L. C., Gailleton, B., & Bruhat, L. (2024). Megathrust
971 locking encoded in subduction landscapes. *Science Advances*, 10(17), eadl4286.
972 <https://doi.org/10.1126/sciadv.adl4286>

973 Perron, J. T., & Royden, L. (2013). An integral approach to bedrock river profile analysis. *Earth*
974 *Surface Processes and Landforms*, 38(6), 570–576. <https://doi.org/10.1002/esp.3302>

975 Ponza, A., Pazzaglia, F. J., & Picotti, V. (2010). Thrust-fold activity at the mountain front of the
976 Northern Apennines (Italy) from quantitative landscape analysis. *Geomorphology*, *123*(3),
977 211–231. <https://doi.org/10.1016/j.geomorph.2010.06.008>

978 Pritchard, D., Roberts, G. G., White, N. J., & Richardson, C. N. (2009). Uplift histories from river
979 profiles. *Geophysical Research Letters*, *36*(24). <https://doi.org/10.1029/2009GL040928>

980 Robert, X., van der Beek, P., Braun, J., Perry, C., Dubille, M., & Mugnier, J.-L. (2009). Assessing
981 Quaternary reactivation of the Main Central thrust zone (central Nepal Himalaya): New
982 thermochronologic data and numerical modeling. *Geology*, *37*(8), 731–734.
983 <https://doi.org/10.1130/G25736A.1>

984 Roberts, G. P., & Michetti, A. M. (2004). Spatial and temporal variations in growth rates along
985 active normal fault systems: an example from The Lazio–Abruzzo Apennines, central Italy.
986 *Journal of Structural Geology*, *26*(2), 339–376. [https://doi.org/10.1016/S0191-](https://doi.org/10.1016/S0191-8141(03)00103-2)
987 [8141\(03\)00103-2](https://doi.org/10.1016/S0191-8141(03)00103-2)

988 Roering, J. J., Kirchner, J. W., & Dietrich, W. E. (1999). Evidence for nonlinear, diffusive sediment
989 transport on hillslopes and implications for landscape morphology. *Water Resources*
990 *Research*, *35*(3), 853–870. <https://doi.org/10.1029/1998WR900090>

991 Roering, J. J., Kirchner, J. W., Sklar, L. S., & Dietrich, W. E. (2001). Hillslope evolution by nonlinear
992 creep and landsliding: An experimental study. *Geology*, *29*(2), 143.
993 [https://doi.org/10.1130/0091-7613\(2001\)029<0143:HEBNCA>2.0.CO;2](https://doi.org/10.1130/0091-7613(2001)029<0143:HEBNCA>2.0.CO;2)

994 Rosenbloom, N. A., & Anderson, R. S. (1994). Hillslope and channel evolution in a marine terraced
995 landscape, Santa Cruz, California. *Journal of Geophysical Research: Solid Earth*, *99*(B7),
996 14013–14029. <https://doi.org/10.1029/94JB00048>

997 Saillard, M., Audin, L., Rousset, B., Avouac, J.-P., Chlieh, M., Hall, S. R., et al. (2017). From the
998 seismic cycle to long-term deformation: linking seismic coupling and Quaternary coastal
999 geomorphology along the Andean megathrust. *Tectonics*, 36(2), 241–256.
1000 <https://doi.org/10.1002/2016TC004156>

1001 Smith, A. G. G., Fox, M., Moore, J. R., Miller, S. R., Goren, L., Morriss, M. C., & Carter, A. (2024).
1002 One Million Years of Climate-Driven Rock Uplift Rate Variation on the Wasatch Fault
1003 Revealed by Fluvial Topography. *American Journal of Science*, 324.
1004 <https://doi.org/10.2475/001c.92194>

1005 Snyder, N. P., Whipple, K. X., Tucker, G. E., & Merritts, D. J. (2000). Landscape response to tectonic
1006 forcing: Digital elevation model analysis of stream profiles in the Mendocino triple
1007 junction region, northern California. *GSA Bulletin*, 112(8), 1250–1263.
1008 [https://doi.org/10.1130/0016-7606\(2000\)112<1250:LRTTFD>2.0.CO;2](https://doi.org/10.1130/0016-7606(2000)112<1250:LRTTFD>2.0.CO;2)

1009 Sreejith, K. M., Sunil, P. S., Agrawal, R., Saji, A. P., Rajawat, A. S., & Ramesh, D. S. (2018). Audit of
1010 stored strain energy and extent of future earthquake rupture in central Himalaya.
1011 *Scientific Reports*, 8(1), 16697. <https://doi.org/10.1038/s41598-018-35025-y>

1012 Steckler, M. S., Mondal, D. R., Akhter, S. H., Seeber, L., Feng, L., Gale, J., et al. (2016). Locked and
1013 loading megathrust linked to active subduction beneath the Indo-Burman Ranges. *Nature*
1014 *Geoscience*, 9(8), 615–618. <https://doi.org/10.1038/ngeo2760>

1015 Su, Q., Xie, H., Yuan, D.-Y., & Zhang, H.-P. (2017). Along-strike topographic variation of Qinghai
1016 Nanshan and its significance for landscape evolution in the northeastern Tibetan Plateau.
1017 *Journal of Asian Earth Sciences*, 147, 226–239.
1018 <https://doi.org/10.1016/j.jseaes.2017.07.019>

1019 Tarantola, A. (2005). *Inverse Problem Theory and Methods for Model Parameter Estimation*.
1020 Society for Industrial and Applied Mathematics.
1021 <https://doi.org/10.1137/1.9780898717921>

1022 Taylor, W. J., & Switzer, D. D. (2001). Temporal changes in fault strike (to 90°) and extension
1023 directions during multiple episodes of extension: An example from eastern Nevada. *GSA*
1024 *Bulletin*, 113(6), 743–759. [https://doi.org/10.1130/0016-](https://doi.org/10.1130/0016-7606(2001)113<0743:TCIFST>2.0.CO;2)
1025 [7606\(2001\)113<0743:TCIFST>2.0.CO;2](https://doi.org/10.1130/0016-7606(2001)113<0743:TCIFST>2.0.CO;2)

1026 Watts, A. B. (2001). *Isostasy and Flexure of the Lithosphere*. Cambridge University Press.
1027 Retrieved from [https://books.google.com/books?hl=en&lr=&id=QIUgBqJ6m-](https://books.google.com/books?hl=en&lr=&id=QIUgBqJ6m-MC&oi=fnd&pg=PR11&dq=isostasy&ots=KMIwT-K-82&sig=EEBi2c-910Do0N-5fBlxEyOtq8)
1028 [MC&oi=fnd&pg=PR11&dq=isostasy&ots=KMIwT-K-82&sig=EEBi2c-910Do0N-](https://books.google.com/books?hl=en&lr=&id=QIUgBqJ6m-MC&oi=fnd&pg=PR11&dq=isostasy&ots=KMIwT-K-82&sig=EEBi2c-910Do0N-5fBlxEyOtq8)
1029 [5fBlxEyOtq8](https://books.google.com/books?hl=en&lr=&id=QIUgBqJ6m-MC&oi=fnd&pg=PR11&dq=isostasy&ots=KMIwT-K-82&sig=EEBi2c-910Do0N-5fBlxEyOtq8)

1030 Weissel, J. K., & Karner, G. D. (1989). Flexural uplift of rift flanks due to mechanical unloading of
1031 the lithosphere during extension. *Journal of Geophysical Research: Solid Earth*, 94(B10),
1032 13919–13950. <https://doi.org/10.1029/JB094iB10p13919>

1033 Wessel, P., Luis, J. F., Uieda, L., Scharroo, R., Wobbe, F., Smith, W. H. F., & Tian, D. (2019). The
1034 Generic Mapping Tools Version 6. *Geochemistry, Geophysics, Geosystems*, 20(11), 5556–
1035 5564. <https://doi.org/10.1029/2019GC008515>

1036 Whipple, K. X. (2009). The influence of climate on the tectonic evolution of mountain belts.
1037 *Nature Geoscience*, 2(2), 97–104. <https://doi.org/10.1038/ngeo413>

1038 Whipple, K. X., & Tucker, G. E. (1999). Dynamics of the stream-power river incision model:
1039 Implications for height limits of mountain ranges, landscape response timescales, and

1040 research needs. *Journal of Geophysical Research: Solid Earth*, 104(B8), 17661–17674.
1041 <https://doi.org/10.1029/1999JB900120>

1042 Willgoose, G., Bras, R. L., & Rodriguez-Iturbe, I. (1991). A physical explanation of an observed link
1043 area-slope relationship. *Water Resources Research*, 27(7), 1697–1702.
1044 <https://doi.org/10.1029/91WR00937>

1045 Williams, P. L., & Cole, J. C. (2007). *Geologic Map of the Albuquerque 30' X 60' Quadrangle, North-*
1046 *central New Mexico* (Vol. 2946). US Department of the Interior, US Geological Survey.
1047 Retrieved from
1048 <https://books.google.com/books?hl=en&lr=&id=SmHuAAAAMAAJ&oi=fnd&pg=PA1&dq>
1049 [=Geologic+Map+of+the+Albuquerque+30%E2%80%99+x+60%E2%80%99+Quadrangle,+](https://books.google.com/books?hl=en&lr=&id=SmHuAAAAMAAJ&oi=fnd&pg=PA1&dq)
1050 [North-Central+New+Mexico&ots=XjNI3pAW57&sig=zlxdaGlePxXrpviuYPt1dkoxExo](https://books.google.com/books?hl=en&lr=&id=SmHuAAAAMAAJ&oi=fnd&pg=PA1&dq)

1051 Wobus, C., Whipple, K. X., Kirby, E., Snyder, N., Johnson, J., Spyropolou, K., et al. (2006). Tectonics
1052 from topography: Procedures, promise, and pitfalls. In S. D. Willett, N. Hovius, M. T.
1053 Brandon, & D. M. Fisher (Eds.), *Tectonics, Climate, and Landscape Evolution* (Vol. 398, p.
1054 0). Geological Society of America. [https://doi.org/10.1130/2006.2398\(04\)](https://doi.org/10.1130/2006.2398(04))

1055 Yanites, B. J., Tucker, G. E., Mueller, K. J., Chen, Y.-G., Wilcox, T., Huang, S.-Y., & Shi, K.-W. (2010).
1056 Incision and channel morphology across active structures along the Peikang River, central
1057 Taiwan: Implications for the importance of channel width. *GSA Bulletin*, 122(7–8), 1192–
1058 1208. <https://doi.org/10.1130/B30035.1>

1059
1060

1061 Supplementary information for
1062 **Inferring Long-Term Tectonic Uplift Patterns from Bayesian Inversion of Fluvially-Incised**
1063 **Landscapes**

1064 **Bar Oryan^{1*}, Boris Gailleton², Jean-Arthur Olive³, Luca C. Malatesta⁴ and Romain Jolivet^{3,5}**
1065
1066

1067 **Affiliations:**

1068 (1)Scripps Institution of Oceanography, UC San Diego, La Jolla, CA 92093,USA

1069 (2)Univ. Rennes, Géosciences Rennes, UMR 6118, 35000 Rennes, France.

1070 (3)Laboratoire de Géologie, École normale supérieure – PSL, CNRS UMR 8538, Paris, France.

1071 (4)Earth Surface Process Modelling, GFZ German Research Center for Geosciences, Potsdam,
1072 Germany.

1073 (5)Institut Universitaire de France, 1 rue Descartes, 75006 Paris.

1074

1075 **Contents of this file**

1076

1077 Text S1 to S4

1078 Figures S1 to S19

1079 Tables S1 to S3

1080

1081 **Additional Supporting Information (Files uploaded separately)**

1082

1083 Code and DEMs used in this manuscript are available at

1084 <https://zenodo.org/records/14029506>

1085

1086

1087

1088 **Text S1 – B Splines**

1089

1090 The B-spline function we used in parametrizing the uplift are described as follow (De Boor,
1091 1978; Piegl & Tiller, 1997):

1092 1. $U(x) = \sum_i^{i+d} Q_i B_{i,d}(x)$

1093 Where Q_i is the spline coefficient controlling the behavior of the B-spline basis function of
1094 order d , $B_{i,d}(x)$, defined recursively in the following way:

1095 2. $B_{i,0}(x) = \begin{cases} 1, & x \in [t_i, t_{i+1}] \\ 0, & elsewhere \end{cases}$

1096
$$B_{i,d}(x) = \frac{x - t_i}{t_{i+d} - t_i} B_{i,d-1}(x) + \frac{t_{i+d+1} - x}{t_{i+d+1} - t_{i+1}} B_{i+1,d-1}(x)$$

1097

1098 t_i is the position of node i .

1099

1100 To describe a two-dimensional uplift patterns we rely on a convolution of B-spline basis
1101 function to describe a surface (De Boor, 1978; Piegl & Tiller, 1997):

1102

1103 3. $U(x, y) = \sum_i^{n+d} \sum_j^{j+d} Q_{i,j} B_{i,d}(x) B_{j,d}(y)$

1104

1105 To compute our uplift function, we distribute nodes along a rectangle uniform grid with
1106 constant spacing along the x and y axis. This enables us to adopt a simpler and computationally
1107 efficient form of B-spline basis (Agrapart & Batailly, 2020). For 1D cubic solution where uplift
1108 varies along the x -axis we use:

1109

1110 4. $U(x) = \frac{1}{6} [u_i^3 \ u_i^2 \ u_i \ 1] \cdot R \cdot \begin{bmatrix} Q_i \\ Q_{i+1} \\ Q_{i+2} \\ Q_{i+3} \end{bmatrix}$

1111

1112 For the 2D case where uplift pattern is a function of x and y we use:

1113

1114 5.
$$U(x, y) = \frac{1}{36} [v_j^3 \ v_j^2 \ v_j \ 1] \cdot R \cdot \begin{bmatrix} Q_{i,j} & Q_{i+1,j} & Q_{i+2,j} & Q_{i+3,j} \\ Q_{i,j+1} & Q_{i+1,j+1} & Q_{i+2,j+1} & Q_{i+3,j+1} \\ Q_{i,j+2} & Q_{i+1,j+2} & Q_{i+2,j+2} & Q_{i+3,j+2} \\ Q_{i,j+3} & Q_{i+1,j+3} & Q_{i+2,j+3} & Q_{i+3,j+3} \end{bmatrix} R^t \begin{bmatrix} \mu_i^3 \\ \mu_i^2 \\ \mu_i \\ 1 \end{bmatrix}$$

1115

1116 Where
$$\mu_i = \frac{x-t_i}{t_{i+1}-t_i}, \quad v_j = \frac{y-t_j}{t_{j+1}-t_j} \quad \text{and } R = \begin{bmatrix} -1 & 3 & -3 & 1 \\ 3 & -6 & 3 & 0 \\ -3 & 0 & 3 & 0 \\ 1 & 4 & 1 & 0 \end{bmatrix}.$$

1117

1118 We note that the numbers of parameters needed is nodes+d(=3) and as we are only interested
1119 in the shape of uplift and normalize our uplift solution between 0 and 1.

1120 Finally, we highlight that our recovered uplift is constrained only by river nodes within our
1121 rectangular domain defining the b-spline surface. Nonetheless, we can extrapolate the uplift
1122 surface across the entire B-spline domain using these parameters. We consider that the
1123 recovered uplift applies only to the basins that feed our selected river nodes, as the water flowing
1124 through these influence the information they provide.

1125

1126

1127

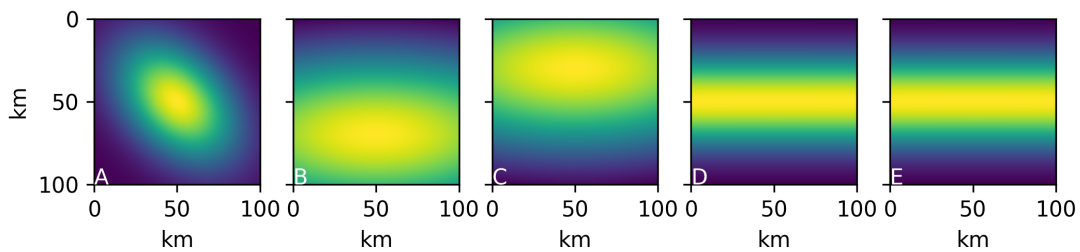
Cases	x_0 [km]	y_0 [km]	σ_x [km]	σ_y [km]	θ [$^\circ$]	Illustration Fig.
Detachment limited, Sediment transportation, Hillslope diffusion (Fig. 1 ,2 and 3)	50	50	30	20	45	1,S2A
Temporal uplift shape (South ridge uplift function ; Fig 5)	50	70	100	40	0	S2B
Temporal change (North ridge uplift function ; Fig 5)	50	30	100	40	0	S2C
Climatic effect & Temporal uplift rate (Figs. 5 & 3)	50	50	1000	20	0	S2D
Erodibility ratio (Fig 6)	50	50	40	25	0	S2E

1128

Table S1 – Imposed tectonic uplift used in synthetic landscape. Uplift functions illustrations are shown in Fig. S1.

1129

1130



1131

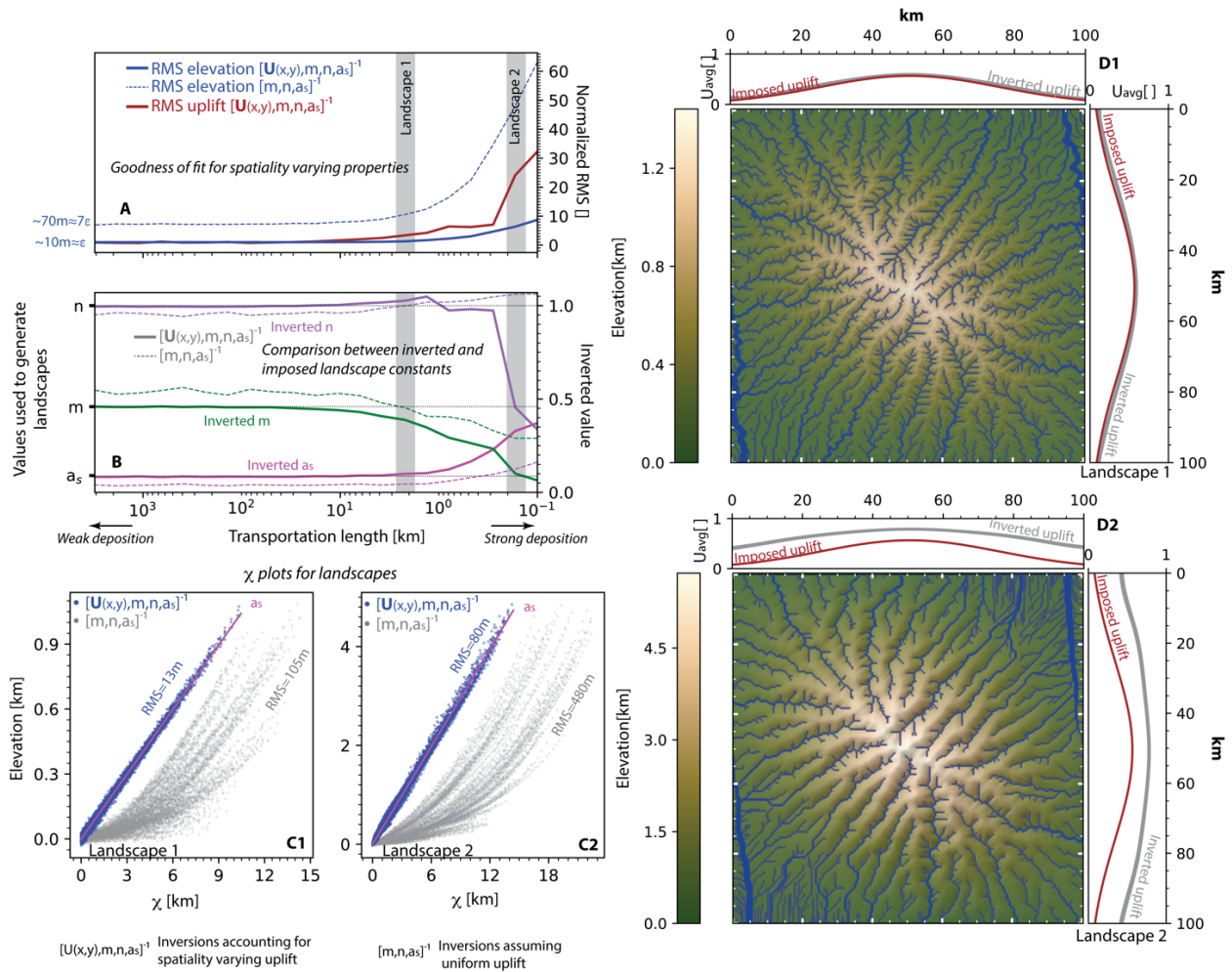
1132

1133

Fig S1 – Uplift imposed for synthetic landscapes cases (see table S1).

1134

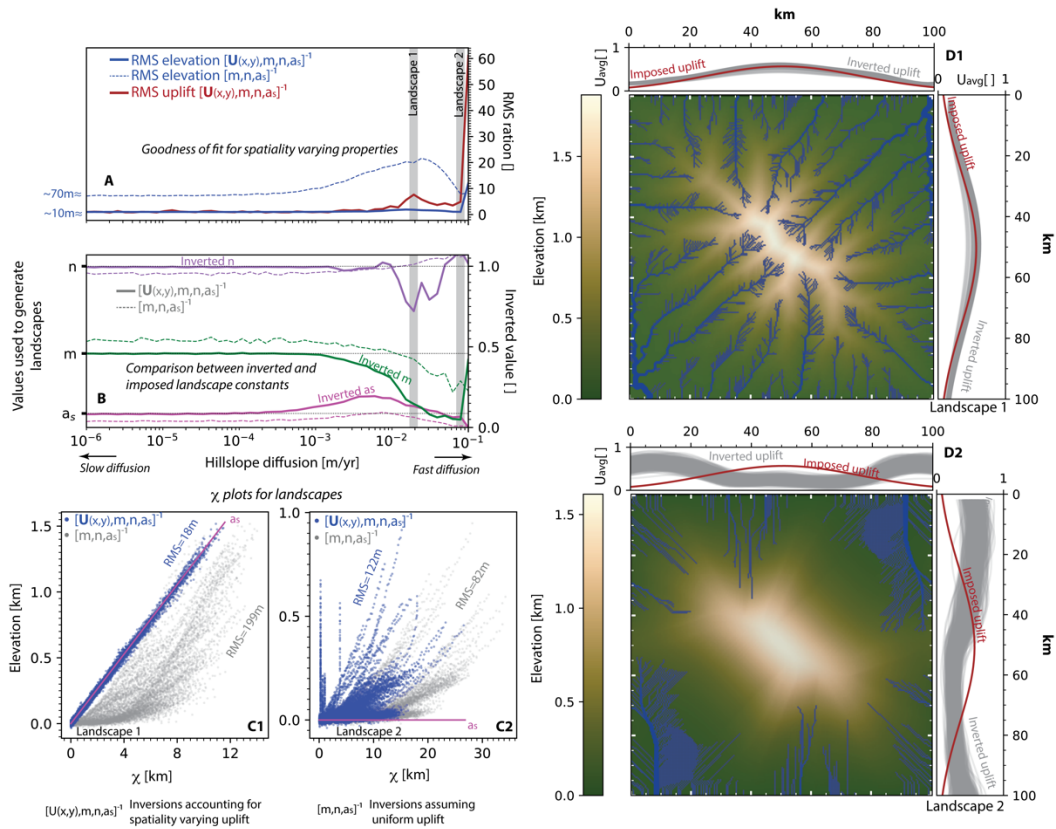
Inverted synthetic landscapes with various degrees of sediment transportation and deposition



1135
 1136
 1137
 1138
 1139
 1140
 1141
 1142
 1143
 1144
 1145
 1146
 1147
 1148
 1149
 1150

Figure S2 – Inverted synthetic landscapes with various degrees of sediment transportation and deposition. Panels A and B show comparison between imposed and recovered landscape properties for inversions of 50 synthetic landscapes, each characterized by a distinct simulated deposition value. A – RMS values for elevation and uplift and normalized with respect to value obtained for the landscape with the weakest deposition. ϵ denote error we introduced amounting to 10m (See section 4.2). B – Comparison between imposed (black dash curve) and mean inverted and m, n and a_s values. Continuous and dashed curves denote inversion results including and excluding uplift, respectively. Grey vertical lines show two landscapes described in panels C and D. C – Points show elevation for 8000 river nodes and χ values derived from best inverted solution. Blue and grey denote inversion results including and excluding uplift, respectively. D – Landscapes Elevation. Blue dots show 8000 river nodes used for the inversion with dot size proportional to the drainage area. Marginal plots show average uplift along axis. Imposed uplift is shown in red curve and 500 samples randomly drawn from the inverted uplift posterior distribution and extrapolated to the domain are shown in grey.

Inverted synthetic landscapes with various degrees of hillslope diffusion



1151

1152 **Figure S3 – Inverted synthetic landscapes with various degrees of hillslope diffusion.**

1153 Panels A,A*,B and B* show comparison between imposed and recovered landscape properties

1154 for inversions of 50 synthetic landscapes, each characterized by a distinct h_o (See section 4.3.5).

1155 Panels with and without an * show outputs for inversions including and excluding the effect of

1156 orographic perception on drainage area, respectively. Blue curves in marginal plots in panels D1

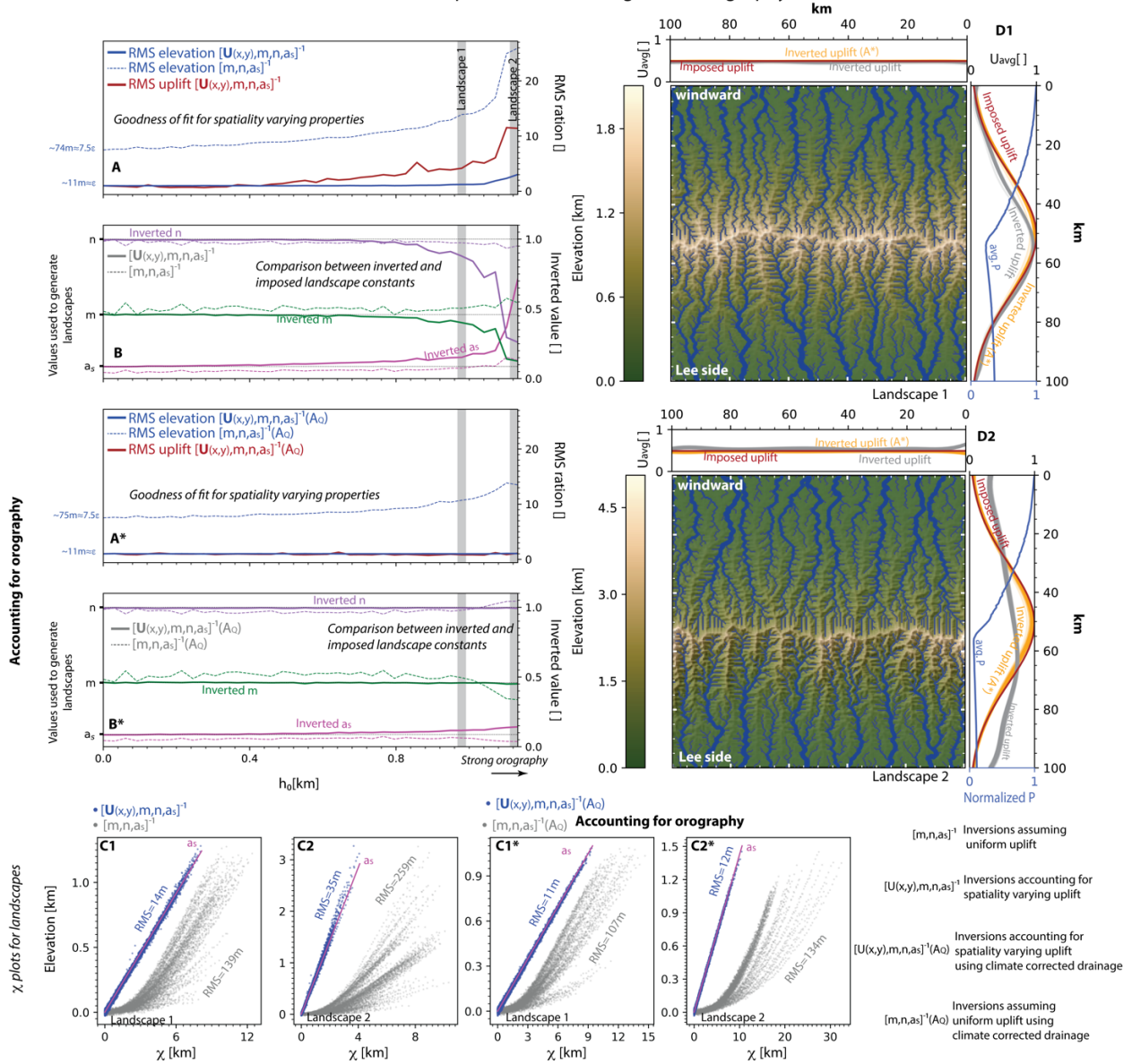
1157 and D2 show the averaged perception along the x axis where 1 and 0 indicate large and negligible

1158 perception, respectively. See Fig. S2 for complete figure description.

1159

1160

Inverted landscapes with various degrees of orography

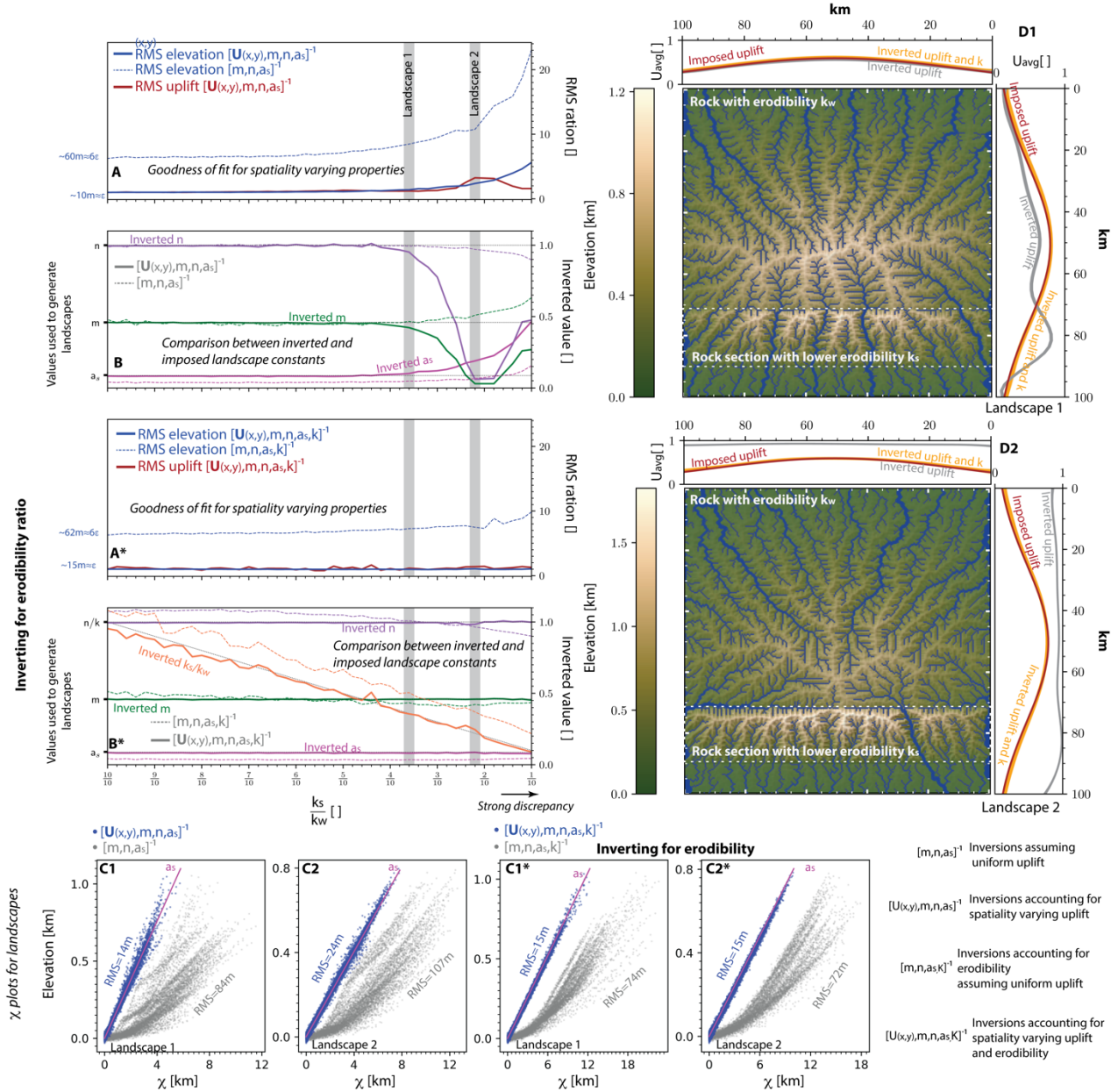


1161
1162
1163
1164
1165
1166
1167
1168
1169
1170
1171

Figure S4 – Inverted synthetic landscapes with various degrees of orographic effect.

Panels A, A*, B and B* show comparison between imposed and recovered landscape properties for inversions of 50 synthetic landscapes, each characterized by a distinct h_o (See section 4.3.5). Panels with and without an * show outputs for inversions including and excluding the effect of orographic perception on drainage area, respectively. Blue curves in marginal plots in panels D1 and D2 show the averaged perception along the x axis where 1 and 0 indicate large and negligible perception, respectively. See Fig. S2 for complete figure description.

Inverted landscapes with various degrees of rock erodibility

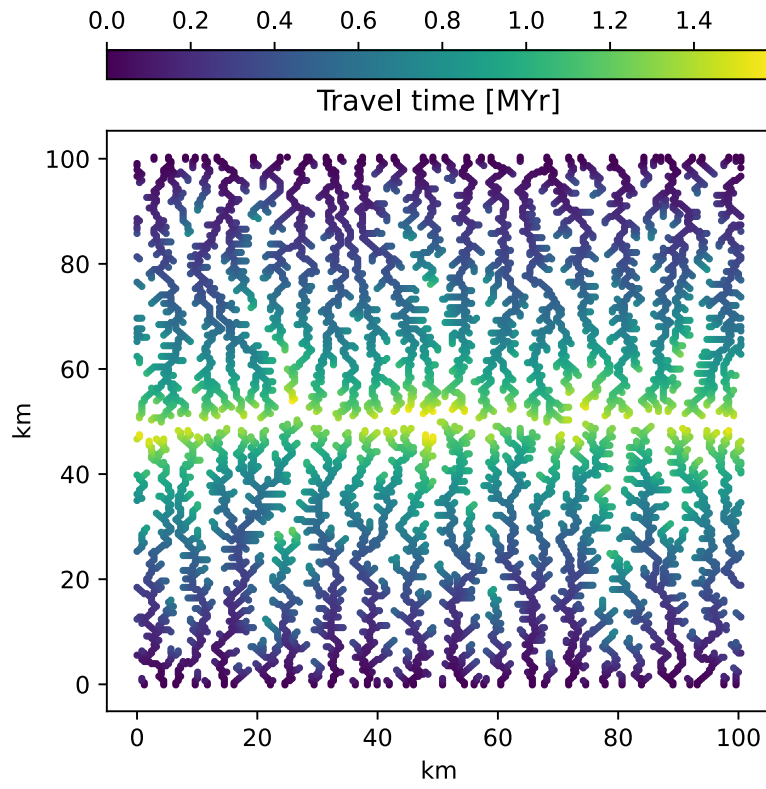


1172
1173

1174 **Figure S5 – Inverted synthetic landscapes with various degrees of rock erodibility.** Panels A, A*, B
1175 and B* show comparison between imposed and recovered landscape properties for inversions
1176 of 50 synthetic landscapes, each characterized by a 20km wide section with a distinct erodibility
1177 value k_s . White dash line in D1 and D2 mark section characterized by erodibility of k_s . Panels
1178 with and without an * show outputs for inversions including and excluding erodibility,
1179 respectively. See Fig. S2 for complete figure description.

1180

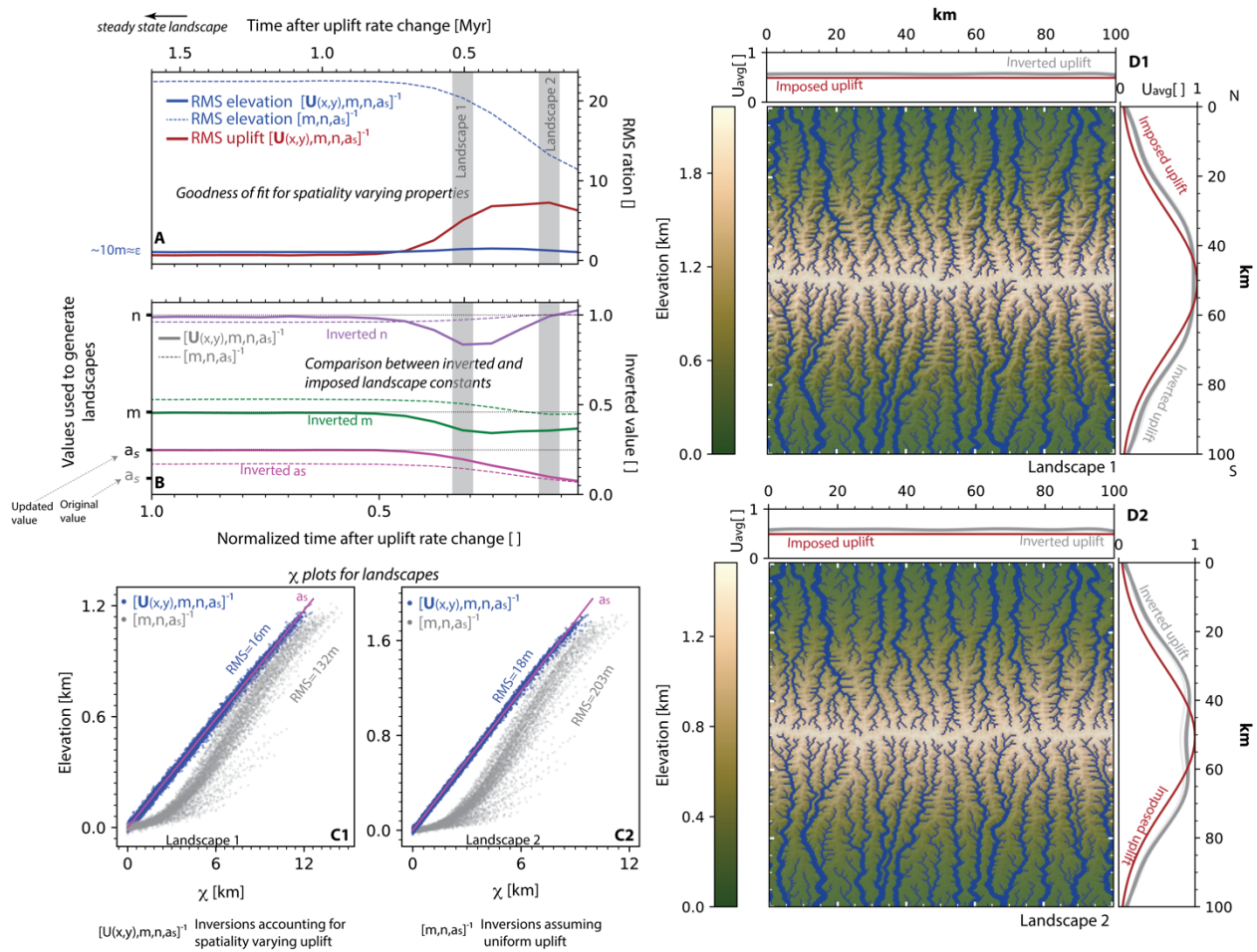
1181
1182



1183
1184
1185
1186

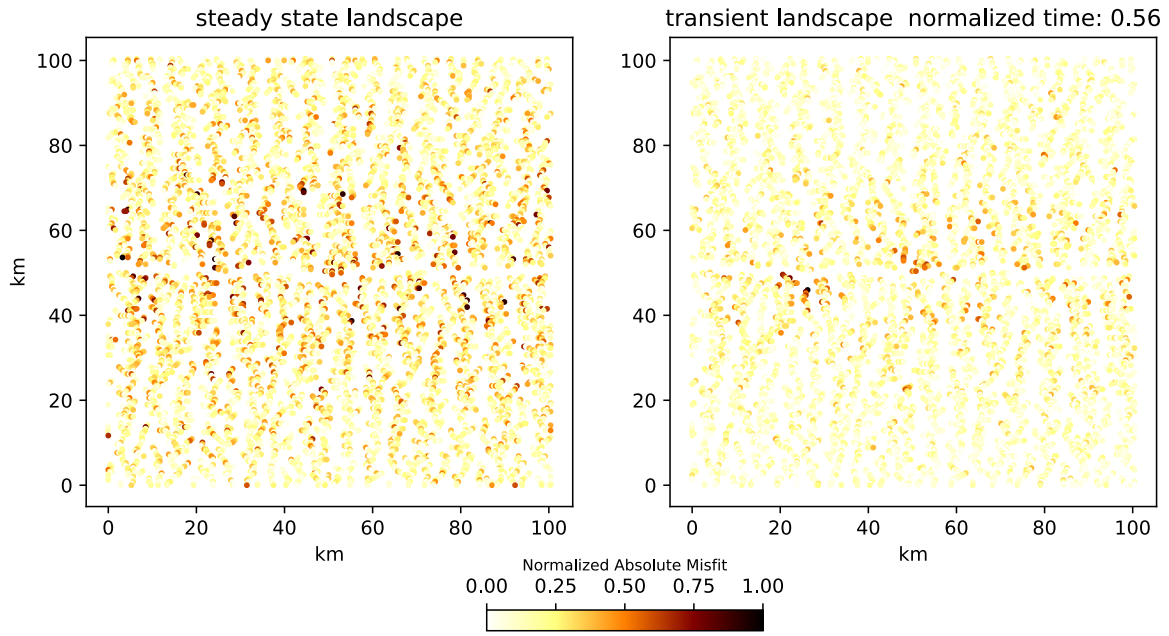
Fig S6– knickpoint travel time from base level to river node.

Inverted landscape following a step change in uplift rate



1187
1188
1189
1190
1191
1192
1193
1194

Figure S7 – Inverted synthetic landscape following an instantaneous change in uplift rate. Panels A and B show comparison between imposed and recovered landscape properties for inversions of snapshots of the landscape at intervals of 0.1 Myr following the step change. Results are presented in time normalized with respect to the duration the landscape requires to reach steady state. See Fig. S2 for complete figure description.



1195
 1196
 1197
 1198
 1199
 1200

Fig S8 – Elevation misfit for two synthetic landscapes. The largest misfit values for the transient landscape are concentrated upstream around the river tips, which have not yet reached equilibrium. In contrast misfits are almost evenly distributed across steady state landscape.

1201 **Text S2 – Synthetic landscape subject to temporal changes in uplift pattern**

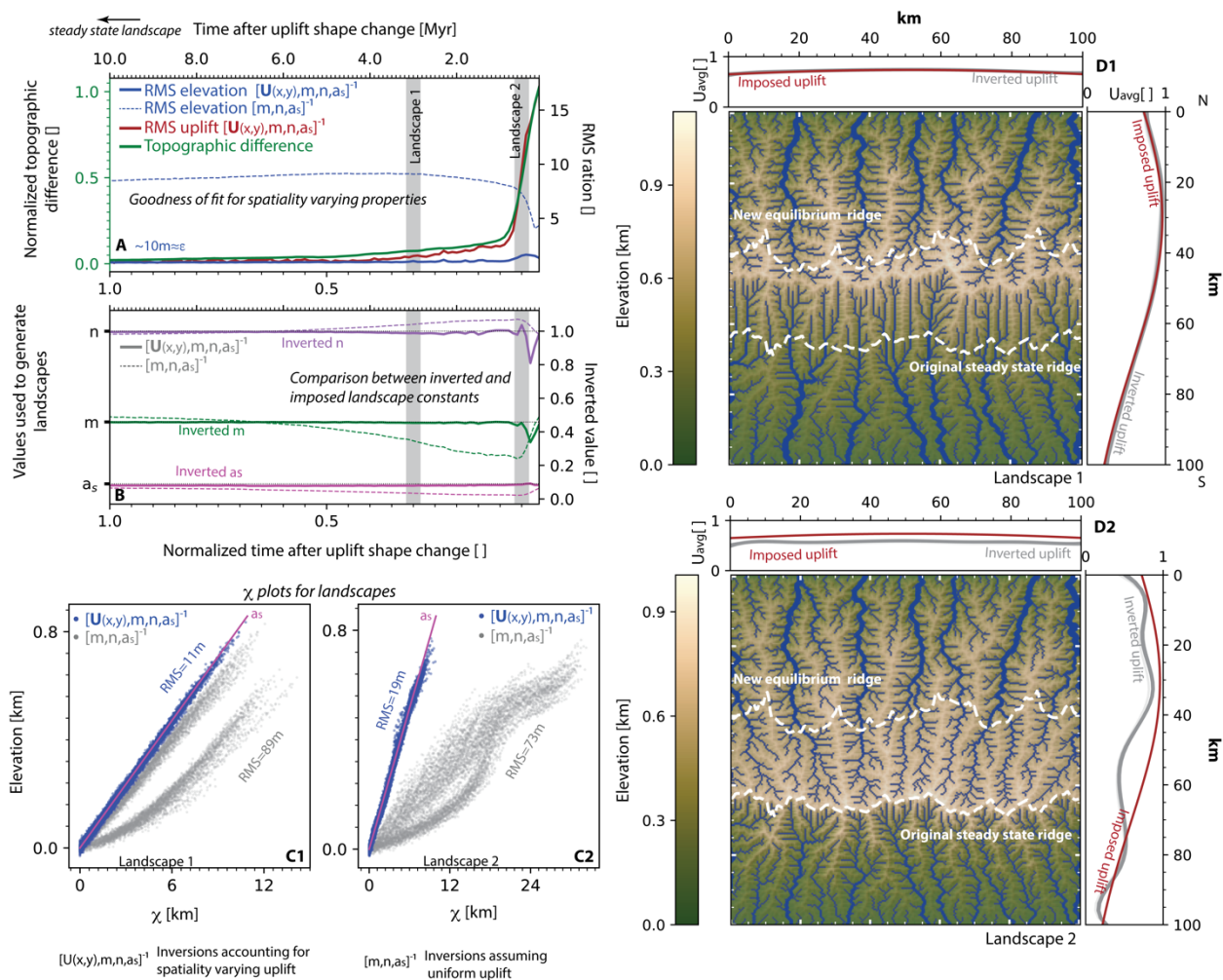
1202

1203 For completeness we examine the effect of temporal changes in uplift pattern (under
1204 constant uplift rate) and simulate a detachment-limited landscape in equilibrium, characterized
1205 by a well-formed east-west mountain range along the southern end of the domain (Fig. 5; Table
1206 S1; Fig. S1). We then introduce a step change in the uplift pattern, resulting in a ~30 km slow
1207 migration of the mountain ridge towards the north (Fig. S9; Table S1; Fig. S1). Following this
1208 instantaneous change, we continue simulating the landscape for an additional 10 million years,
1209 performing inversions on landscape snapshots recorded at intervals of 0.1 million years.

1210 Due to the nonlinearity and complexity of the signal we introduce (Royden & Taylor
1211 Perron, 2013; Steer, 2021), we estimate the time for the landscape to reach a new equilibrium
1212 by computing the mean of the absolute differences in topographic height across successive
1213 timesteps (green curve, Fig. S9A). Approximately 10 million years following the step change, the
1214 ridge stabilizes at its final position, with mean topographic change diminishing to about 1% of its
1215 maximum value post-change (Fig. S9A).

1216 The inverted and recorded elevations align almost perfectly, while other landscape
1217 properties show more pronounced errors (Figs. S9A & S9B). This consistency in elevation retrieval
1218 suggests that the inversion effectively compensates with adjustments in other parameters to
1219 return accurate elevation values. This is because the transient signals are primarily driven by
1220 detachment-limited processes, in contrast to sediment deposition and hillslope diffusion. This
1221 illustrates the challenge of determining whether a natural landscape, lacking direct constraints
1222 on uplift and landscape constants, is in steady state based solely on elevation errors. Additional
1223 similarity with scenario (1) is that the recovered uplift almost perfectly matches the imposed
1224 uplift by about half the dimensionless time, significantly earlier than when the landscape reaches
1225 its final equilibrium. This is particularly notable given that the ridge still needs to migrate
1226 approximately 10 km before reaching its steady state position (Figs. S9D1 & S9D2).

Inverted landscape following a step change in uplift shape



1227 **Figure S9 – Inverted synthetic landscape following an instantaneous change in uplift shape.**
 1228
 1229 Panels A and B show comparison between imposed and recovered landscape properties for
 1230 inversions of snapshots of the landscape at intervals of 0.1 Myr following the step change. Results
 1231 are presented in time normalized with respect to the duration the landscape requires to reach
 1232 steady state. Green curve shows the normalized mean topographic difference computed
 1233 between successive timesteps. Dashed white lines show the original and new positions of the
 1234 ridge in steady state. See Fig. 2 for complete figure description.
 1235
 1236

1237

1238

1239 Table S2 – Properties of natural landscapes. *Olive et al., 2022 and references therein. **Ellis &
 1240 Barnes, 2015 and references therein. ^ See text S5.

1241

	Base altitude for χ [m]	Min drainage area [km^2]	Master fault UTM coordinates (x1, y1) and (x2, y2) (m) + UTM zone *	Knots Used for inversion	Brittle layer thickness[km]*	u_0 [$\frac{mm}{yr}$]	Age of onset [Myr]
Paeroa Range, New Zealand (A)	400	2.5	(4.3843e5, 5.7567e6) (4.3115e5, 5.7487e6) UTM 60H	1	6-8	1.5**	1-0.9**
Sandia Mountains, New Mexico, USA (B)	2100	2	(3.6423e5, 3.8973e6) (3.6452e5, 3.8866e6) UTM 13N	1	7-10	0.14^	22^
Wassuk Range, Nevada, USA (C)	1500	1	(3.4679e5,4.2762e6) (3.4620e5,4.2968e6) UTM 11S	4	11-14	0.6**	15**
Kipengere Range / N.E. shores of Lake Malawi, Tanzania (D)	550	1	(6.1128e5, 8.9515e6) (6.6862e5, 8.8871e6) UTM 36L	7	32-37	0.12^	23^
Lemhi Range, Idaho, USA (E)	2200	3	(2.6519e5, 4.9486e6) (2.875e5, 4.9305e6) UTM 12T	Kx=2 ky=3	12-16	0.5**	6.5**
Himalayas	550	10	UTM 45N	Kx=9; ky=9			

1242

1243 **Text S2 - Akaike Information Criterion**

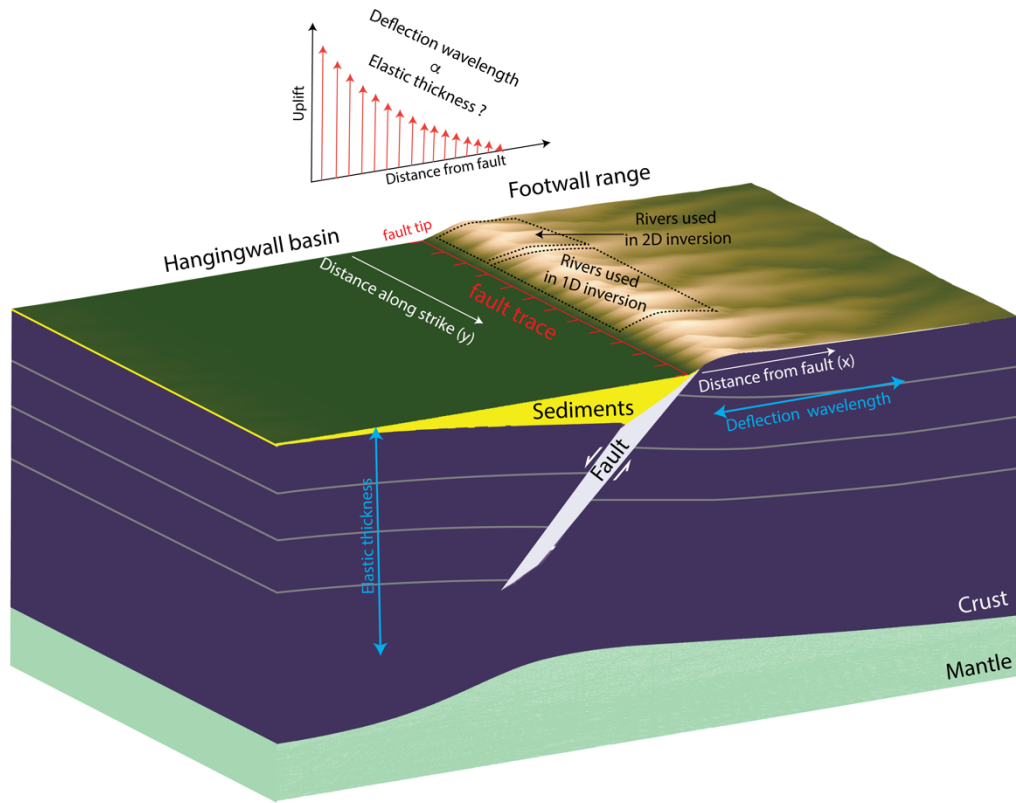
1244

1245 The Akaike Information Criterion is a method used in statistics to determine the relative quality
1246 of statistical models for a given set of data. It is calculated using the formula:

1247
$$AIC = 2(k - \ln(L))$$

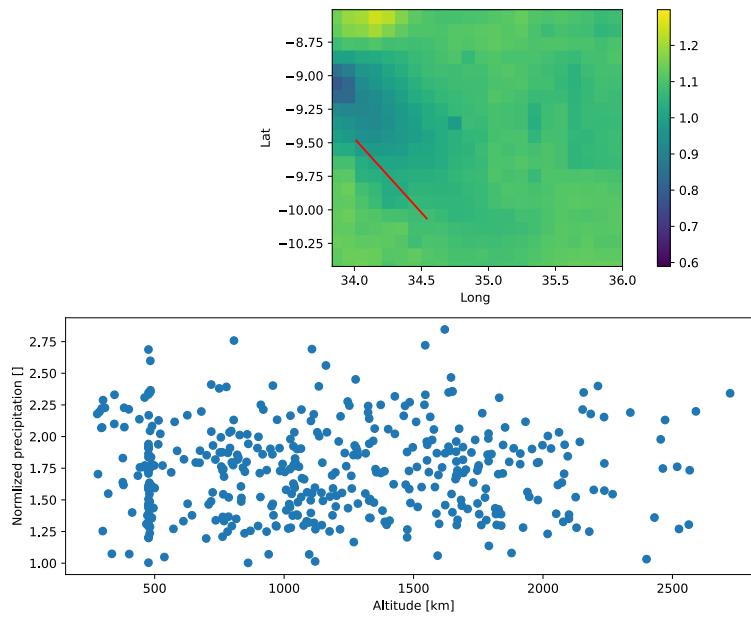
1248 where k is the number of parameters in the model and L is the maximum value of the likelihood
1249 function for the model.

1250

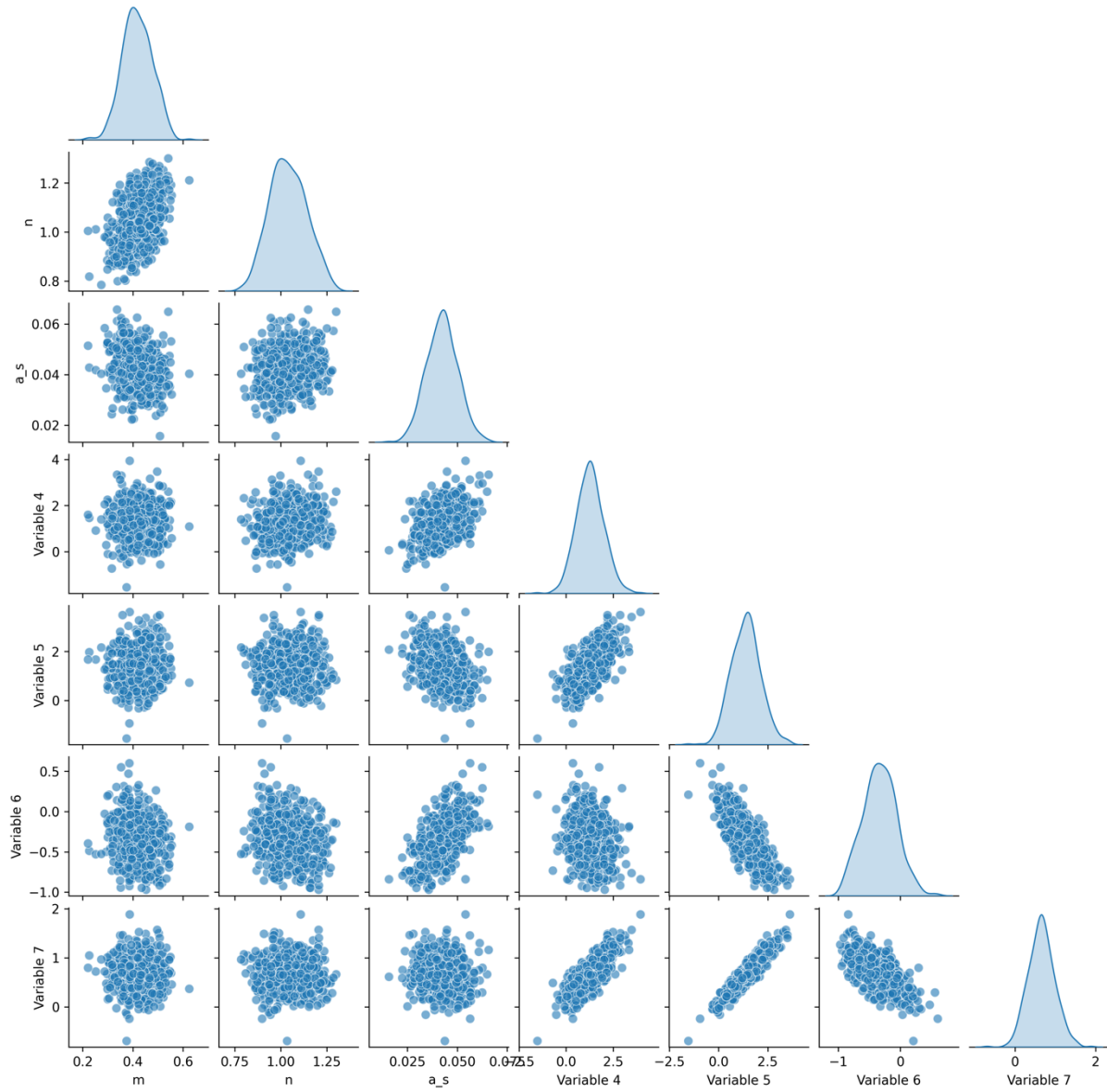


1251
 1252
 1253
 1254
 1255
 1256

Figure S10 – Illustration showing the deflation of the lithosphere and resulting landscape due to offset accommodated along a half graben normal fault system.



1257
1258 Fig S11 – Upper panel – Standard deviation of precipitation divided by the average precipitation
1259 per pixel for rainfall data collected over 23 years from November 1, 2000, by the GPM mission
1260 (Huffman et al., 2015). The red line indicates the position of the Livingston normal fault (Fig S8).
1261 Lower panel - Elevation and average precipitation for 418 data points corresponding to the
1262 rainfall data shown in the upper panel.
1263



1265

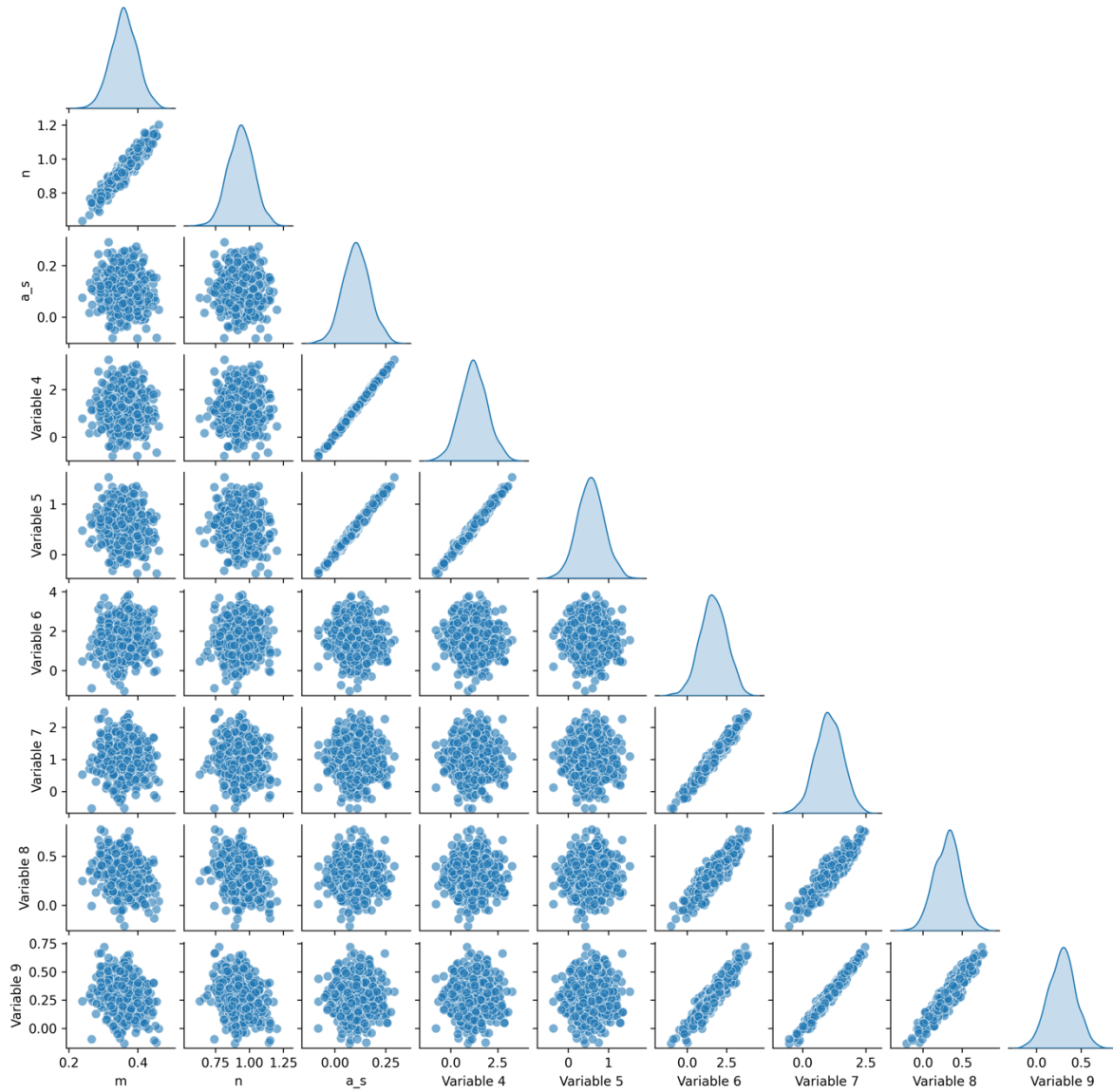
1266

1267

Figure S12 - Pair plots for the New Zealand landscape. Variables 4-7 indicate parameters controlling the b-spline functions. These were estimated using 500 samples randomly drawn

1268 from the posterior distribution.

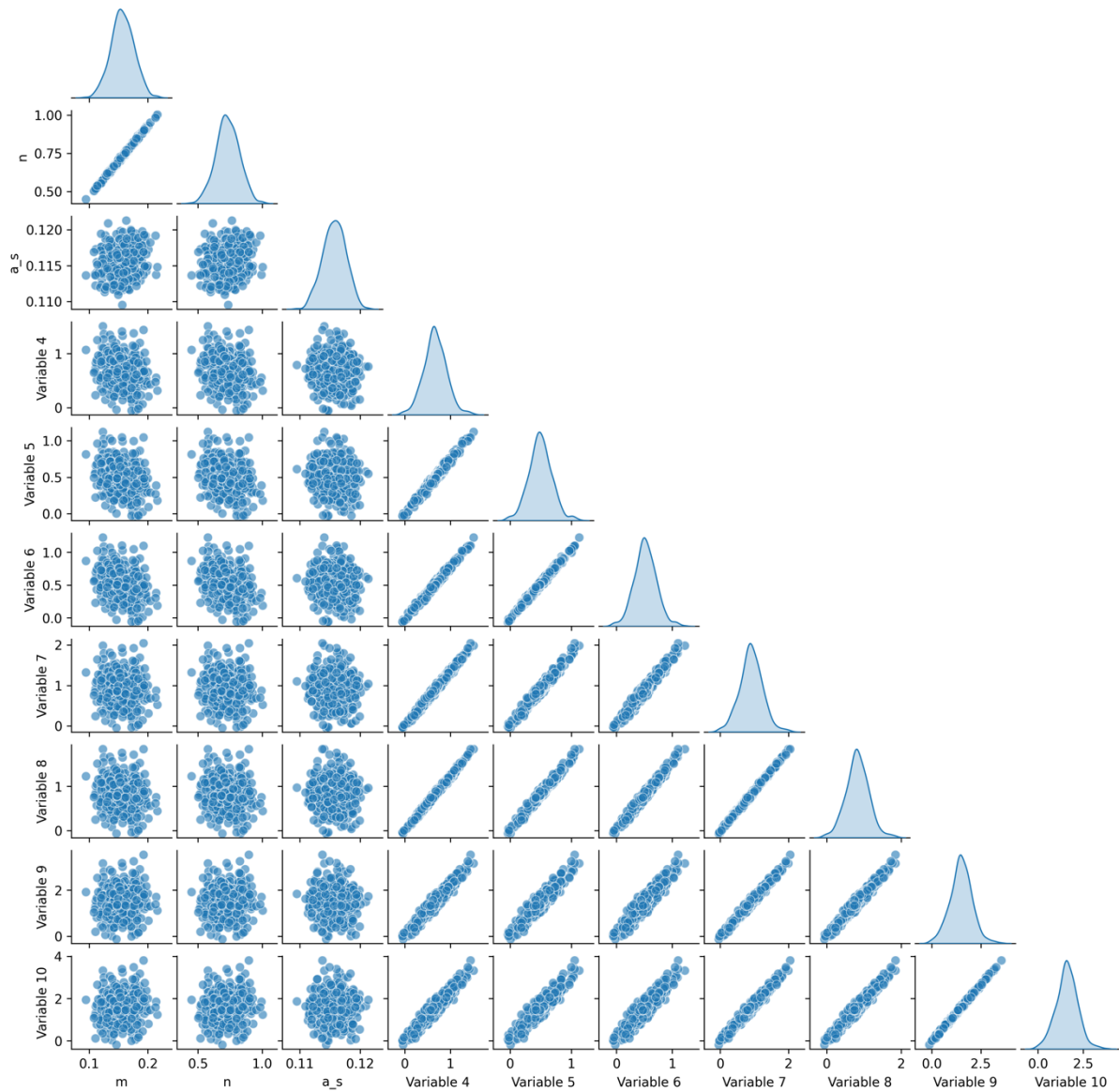
Sandia



1269

1270 Figure S13 - Pair plots for the Sandia landscape. Variables 4-5 and 6-9 indicate parameters
1271 controlling the erodibility and b-spline functions, respectively. These were estimated using 500
1272 samples randomly drawn from the posterior distribution.

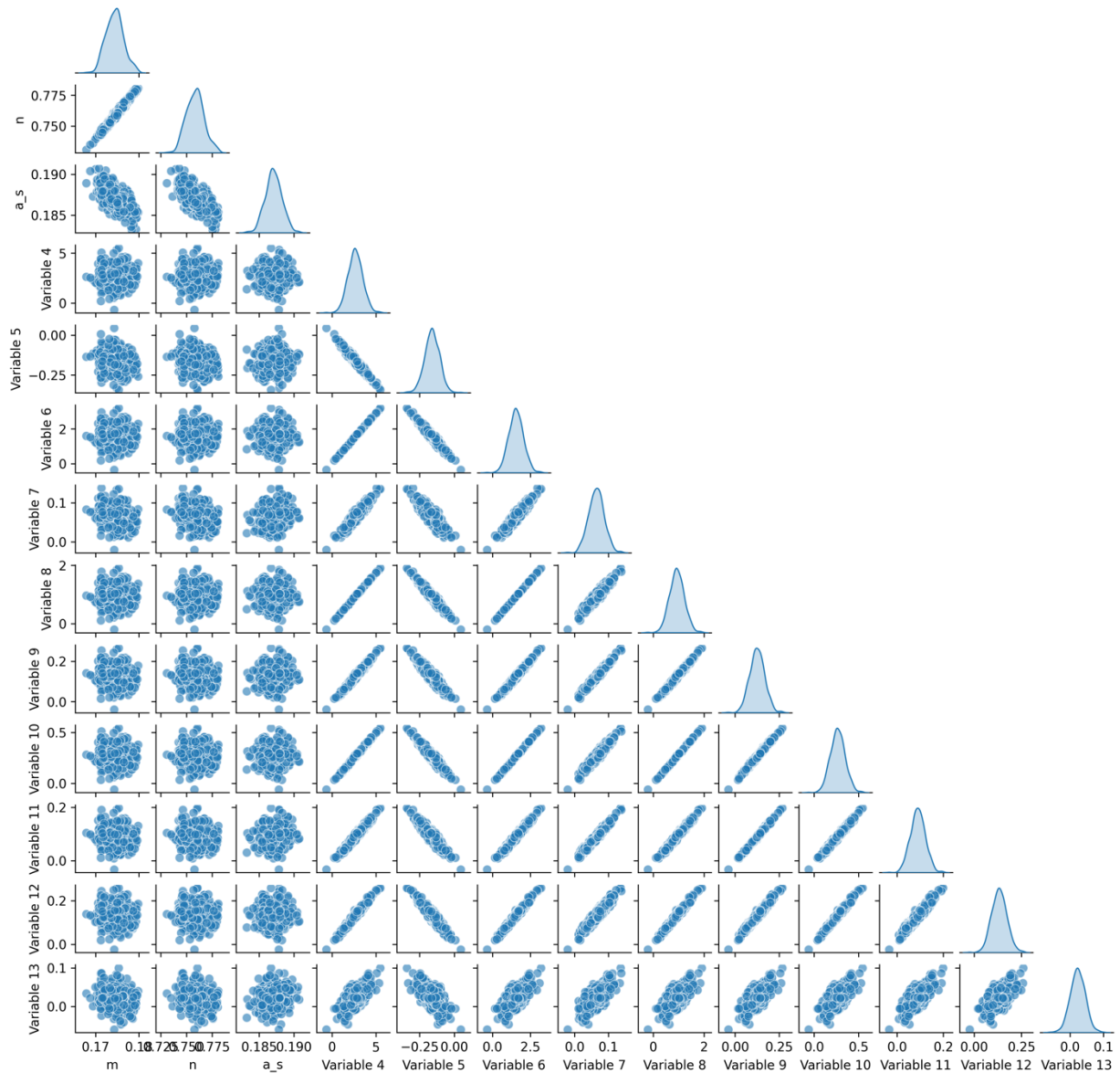
Wassuk



1273
1274
1275
1276

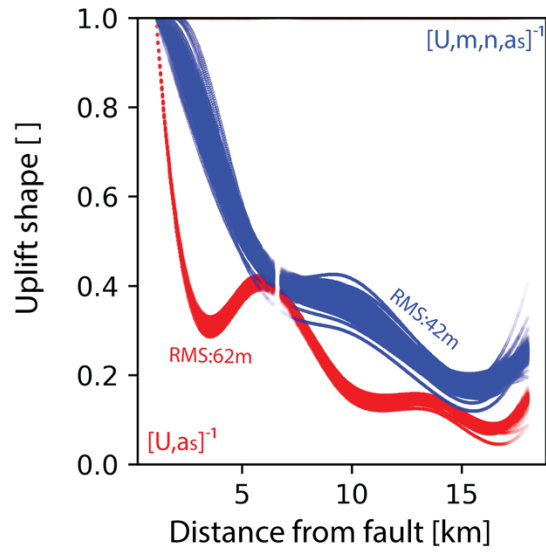
Figure S14 - Pair plots for the Wassuk landscape. Variables 4-10 indicate parameters controlling the b-spline functions. These were estimated using 500 samples randomly drawn from the posterior distribution.

Malwai



1277
1278
1279
1280
1281
1282

Figure S15 - Pair plots for the Malwai landscape. Variable 4-13 indicate parameters controlling the b-spline functions. These were estimated using 500 samples randomly drawn from the posterior distribution.



1283
 1284
 1285
 1286
 1287

Fig S16 – Comparison of uplift solutions for Wassuk Range for the case the inversion is fixed at $m=0.45$ and $n=1$. Colored curve show 500 uplift solutions randomly sampled from our posterior distributions.

1288

	Tethyan Sedimentary Sequence (TTS)	Upper Greater Himalayan Sequence (UGS)	Lesser Himalayan Sequence (LHS)	Lower Greater Himalayan Sequence (LGHS)
Relative erodibility value	0.88 ± 0.40	1.19 ± 0.54	1.01 ± 0.46	0.87 ± 0.39

1289 Table S3 – Best-fitting and standard deviation of relative erodibility values for the Himalayan
1290 inversion including the climate effect.

1291

1292 **Text S3 – Further exploration of temporally varying uplift rates**

1293

1294

1295

1296

1297

1298

1299

1300

1301

To investigate the impact of variable uplift rates, we modeled 29 landscapes, each initially at steady state under a uniform uplift rate of 1.2 mm/year. We then simulated each landscape over an additional 400K years, during which uplift rates linearly adjusted to final values between 12 and 0.12 mm/year (Fig. S12). This 400K-year period is designed to reflect the fastest changes in uplift rate recorded along Utah's Wasatch Fault (Smith et al., 2024). Throughout this time interval, we retained and inverted 12 landscape snapshots, allowing us to assess the temporal variation in landscape response. The results we present are averaged from these 12 landscape analyses.

1302

1303

1304

1305

1306

1307

1308

1309

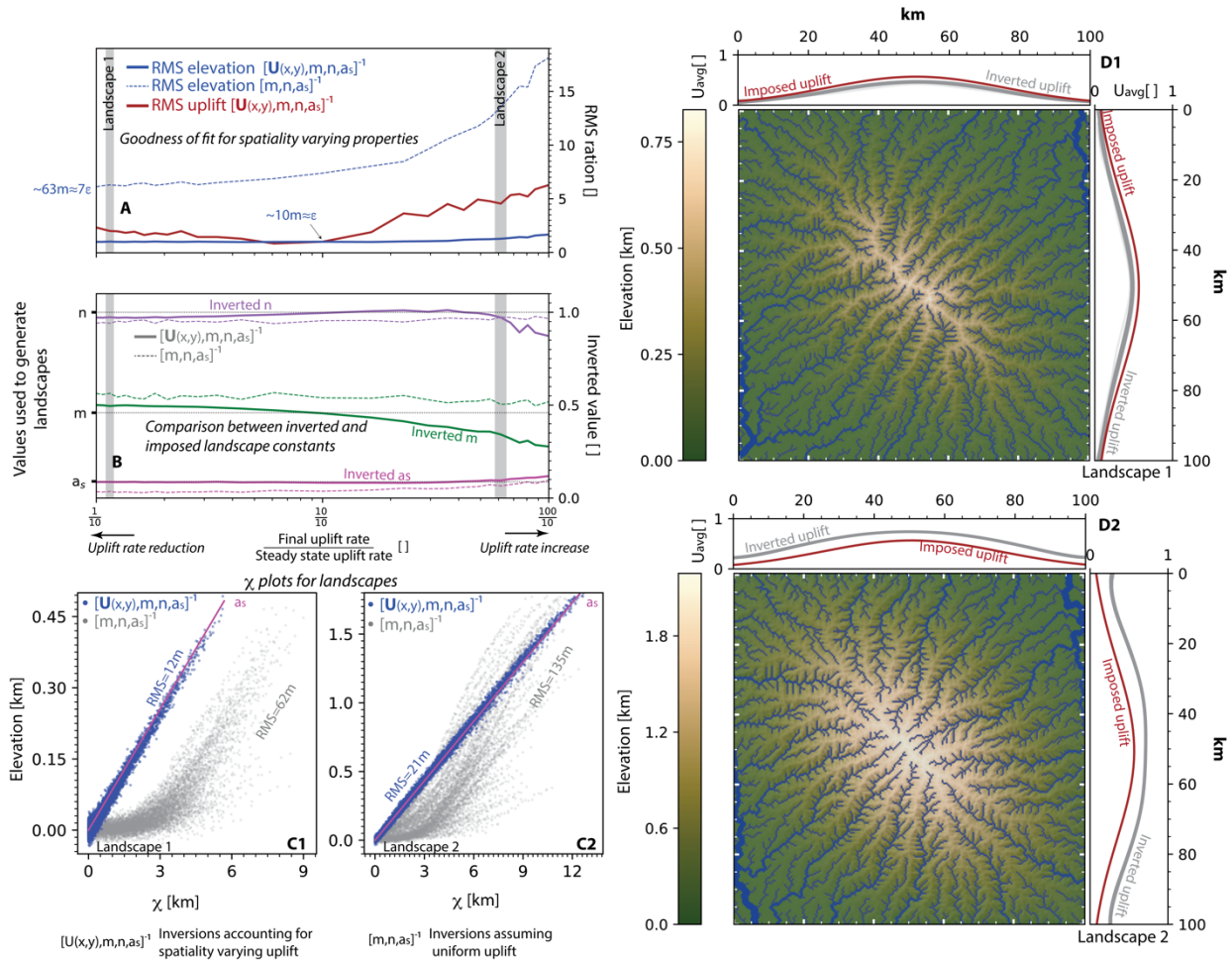
1310

1311

1312

Our inversion reveals that greater contrasts in uplift rates lead to pronounced deviations from the imposed landscape properties. For instance, a tenfold increase in uplift rate results in RMS values ranging from 3 to 7 times larger than the baseline (Fig. S12). Notably, landscapes experiencing an increase in uplift rate exhibit RMS values approximately twice as large as those undergoing a decrease (Fig. S12A). This difference likely stems from the landscape's delayed response in adjusting to reduced rock removal at lower uplift rates. The erodibility of the rock affects this asymmetry, with higher erodibility potentially reversing the trend. Despite less precision with significant uplift increases, the inversion still accurately captures the uplift pattern, albeit with a slight, consistent deviation from the imposed configuration (Figs. S12D1 & S12D2).

Inverted synthetic landscapes with various degrees of uplift rate change



1313

1314

1315 **Figure S17 – Inverted synthetic landscapes with varying degrees of temporal changes in**

1316 **imposed tectonic uplift rate.** Panels A and B show comparison between imposed and recovered

1317 landscape properties for inversions of 50 synthetic landscapes, each characterized by a distinct

1318 final uplift rate value employed in simulating the landscape. Values shown in panels A and B are

1319 averaged for 12 snapshots of the landscape during the 400K years over which the change in rate

1320 occurred. Panels C & D show the results for the last time step of the tectonic rate change. See

1321 Fig. 2 for complete figure description.

1322

1323

1324

1325 **Text S4 – Further exploration of temporally varying uplift shape**

1326

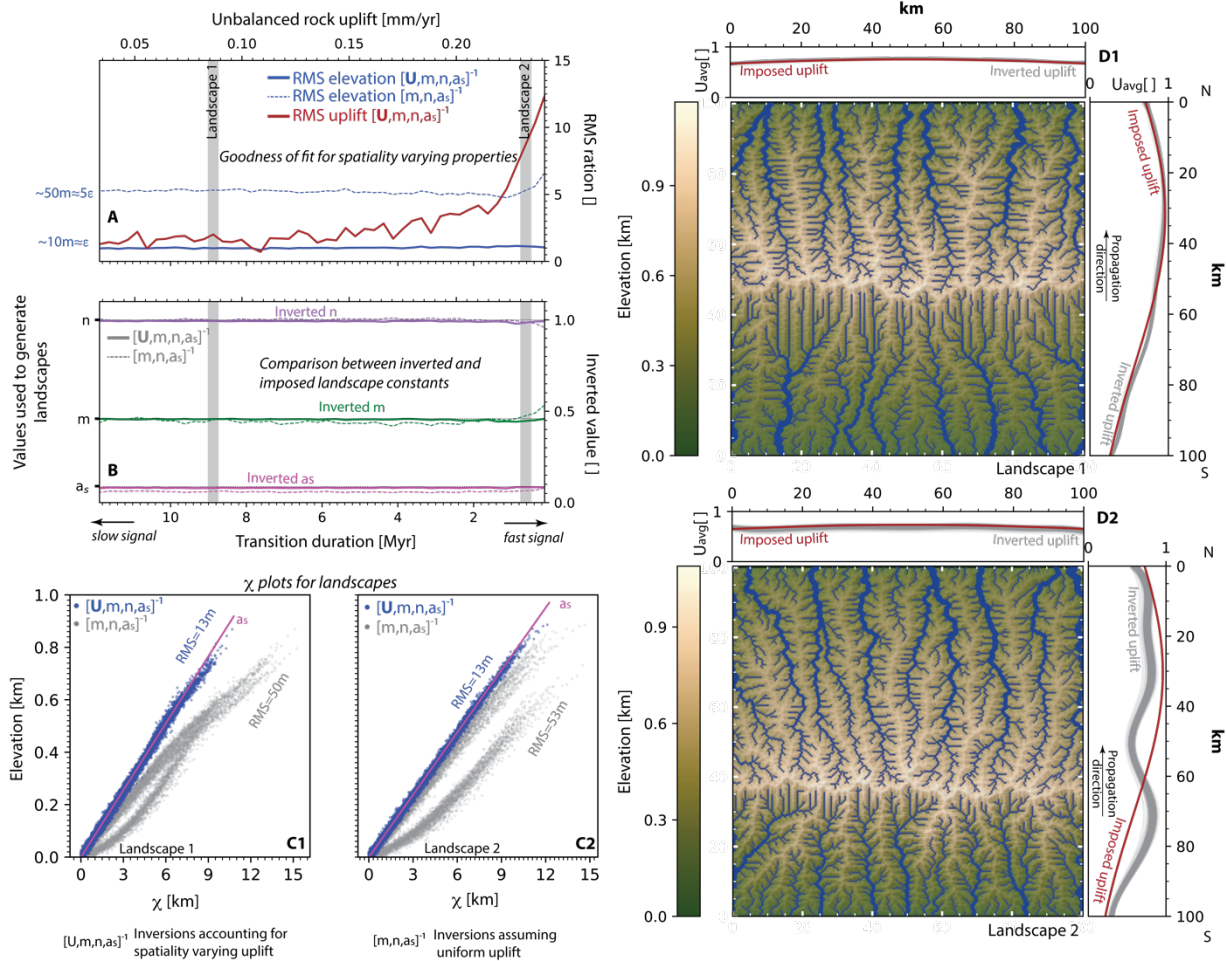
1327

1328 We modeled 48 landscapes that initially reach a topographic steady state, featuring an
1329 uplifting domain along the southern edge of the model (Table S1; Fig. S1). We then reduce uplift
1330 rate along the southern edge while commensurably increasing it along the northern edge,
1331 causing the mountain range to migrate north (e.g., Fig S13D1). Each landscape is associated with
1332 a distinct migration period ranging 120K to 12 M years (Figs. S13 & S1; Table S1). We report the
1333 average results for retained 12 snapshots of each landscape intervals during this migration
1334 process.

1335 The inversion results in realistic inversion outputs with elevation RMS values only a few
1336 meters higher than ε when the timescale of tectonic changes is ≥ 6 Myr (Figs. S13A, S13B &
1337 S13D1). In contrast, faster temporal changes, which build synthetic topography at rate of at least
1338 $0.17 \text{ mm} \cdot \text{yr}^{-1}$ results in inverted uplift showing increasingly larger deviation from imposed
1339 uplift (Figs S13A & S13B).

1340

Inverted landscapes with various degrees of transient uplift pattern



1341

1342

Figure S18 – Inverted synthetic landscapes subject to varying temporal changes in the imposed tectonic uplift pattern. Panels A and B show comparison between imposed and recovered landscape properties for inversions of 50 synthetic landscapes, each characterized by a distinct duration of north migrating uplift signal value. Values shown in panels A&B are averaged for 12 snapshots of the landscape during the migration processes while panels C & D show the results for the last time step of the tectonic migration. See Fig. 2 for complete figure description.

1348

1349

1350

1351 **Text S5 – Estimating k_0 and knickpoint travel time**

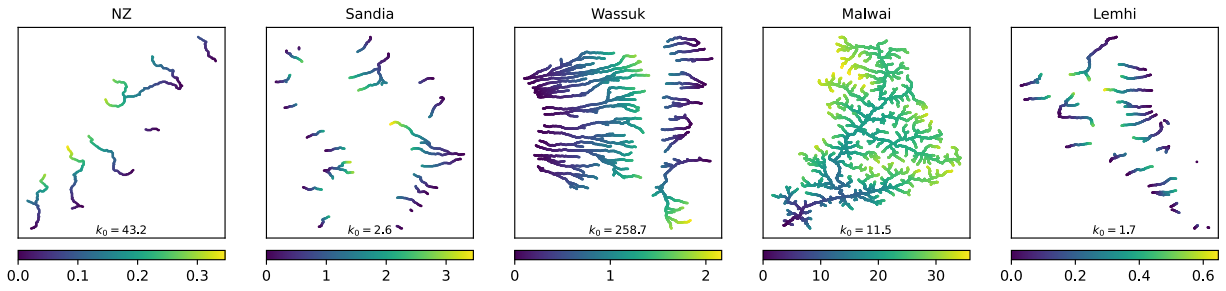
1352 We use our inverted m, n, a_s and previous estimations of u_0 (Table S2; Ellis & Barnes, 2015) to
1353 retrieve k_0 using $k_0 = \frac{u_0}{a_s^n A_0^m}$. For Lake Malawi and Sandia landscapes, where direct uplift rate
1354 estimations are unavailable, we follow Ellis & Barnes (2015) and estimate the minimum uplift
1355 rate using timing of fault initiation and a linear scaling relationship between fault displacement
1356 and length (Schlische et al., 1996)

1357 Lake Malawi and the Kipengere Range, known as the Livingstone Mountains, have formed
1358 due to flexural-isostatic rebound in response to localized extension at the southern end of the
1359 East African Rift. High-resolution seismic imaging of sediments deposited in the northern basin
1360 of Lake Malawi along the ~80km long Livingstone Fault, the focus of our analysis, suggests a fault
1361 displacement (throw) of between 6.6 and 7.4 km. (Accardo et al., 2018). Apatite
1362 thermochronology along the Livingstone fault system indicates that regional cooling, associated
1363 with the onset of Cenozoic rifting, started approximately 23 million years ago (Mortimer et al.,
1364 2016). This results in uplift rate of $0.12 \text{ mm} \cdot \text{yr}^{-1}$.

1365 The Sandia fault delineates the steep western face of the Sandia Mountains and marks
1366 the eastern boundary of the Albuquerque basin part of the Rio Grande Rift. Apatite fission track
1367 (AFT) and (U-Th)/He data from the Sandia Mountains indicate fault activity and rapid cooling 22-
1368 17Ma (House et al., 2003). Using fault length of 100km (McCalpin & Harrison, 2006) we estimate
1369 minimum uplift rate of $0.14 \text{ mm} \cdot \text{yr}^{-1}$.

1370 Finally, we use equation (3) to compute knickpoint travel time from the base level (Fig. S13). We
1371 would like to note that we calculate the drainage pattern assuming a uniform precipitation rate
1372 of $1 \text{ m} \cdot \text{yr}^{-1}$, which is generally a reasonable value except for the Sandia and Wassuk regions
1373 where rainfall is lower. However, we disregard this effect as these landscapes are in a steady
1374 state, and lowering the uniform precipitation rate would reduce A_0 , leading to even faster travel

1375 times.



1376

1377 Fig S19 – Travel time in million years for the five natural landscapes used in the study. Colormap
1378 shows travel time from river base. k_0 shows 10^{-6} erodibility values.

1379

1380

1381

1382

1383 **References**

- 1384
- 1385 Accardo, N. J., Shillington, D. J., Gaherty, J. B., Scholz, C. A., Nyblade, A. A., Chindandali, P. R. N.,
- 1386 et al. (2018). Constraints on Rift Basin Structure and Border Fault Growth in the Northern
- 1387 Malawi Rift From 3-D Seismic Refraction Imaging. *Journal of Geophysical Research: Solid*
- 1388 *Earth*, 123(11), 10,003-10,025. <https://doi.org/10.1029/2018JB016504>
- 1389 Agrapart, Q., & Batailly, A. (2020). Cubic and bicubic spline interpolation in Python. *École*
- 1390 *Polytechnique de Montréal.*, 52. <https://doi.org/ffhal-03017566v2>
- 1391 De Boor, C. (1978). *A practical guide to splines* (Vol. 27). springer-verlag New York. Retrieved from
- 1392 [https://www.researchgate.net/profile/Carl-De-](https://www.researchgate.net/profile/Carl-De-Boor/publication/200744645_A_Practical_Guide_to_Spline/links/02e7e51700ff60945400000/A-Practical-Guide-to-Spline.pdf)
- 1393 [Boor/publication/200744645_A_Practical_Guide_to_Spline/links/02e7e51700ff6094540](https://www.researchgate.net/profile/Carl-De-Boor/publication/200744645_A_Practical_Guide_to_Spline/links/02e7e51700ff60945400000/A-Practical-Guide-to-Spline.pdf)
- 1394 [00000/A-Practical-Guide-to-Spline.pdf](https://www.researchgate.net/profile/Carl-De-Boor/publication/200744645_A_Practical_Guide_to_Spline/links/02e7e51700ff60945400000/A-Practical-Guide-to-Spline.pdf)
- 1395 Ellis, M. A., & Barnes, J. B. (2015). A global perspective on the topographic response to fault
- 1396 growth. *Geosphere*, 11(4), 1008–1023. <https://doi.org/10.1130/GES01156.1>
- 1397 House, M. A., Kelley, S. A., & Roy, M. (2003). Refining the footwall cooling history of a rift flank
- 1398 uplift, Rio Grande rift, New Mexico. *Tectonics*, 22(5).
- 1399 <https://doi.org/10.1029/2002TC001418>
- 1400 McCalpin, J., & Harrison, J. B. J. (2006). *Paleoseismicity of the Sandia Fault Zone, Albuquerque,*
- 1401 *New Mexico.* GEO-HAZ Consulting Crestone, Colorado. Retrieved from
- 1402 [https://geohaz.com/downloads/CONTRACT%20RPTs/2006%20Sandia%20fault%20NM%](https://geohaz.com/downloads/CONTRACT%20RPTs/2006%20Sandia%20fault%20NM%20LowRes.pdf)
- 1403 [20LowRes.pdf](https://geohaz.com/downloads/CONTRACT%20RPTs/2006%20Sandia%20fault%20NM%20LowRes.pdf)
- 1404 Mortimer, E., Kirstein, L. A., Stuart, F. M., & Strecker, M. R. (2016). Spatio-temporal trends in
- 1405 normal-fault segmentation recorded by low-temperature thermochronology: Livingstone

1406 fault scarp, Malawi Rift, East African Rift System. *Earth and Planetary Science Letters*, 455,
1407 62–72. <https://doi.org/10.1016/j.epsl.2016.08.040>

1408 Piegel, L., & Tiller, W. (1997). *The NURBS Book*. Springer-Verlag.

1409 Schlische, R. W., Young, S. S., Ackermann, R. V., & Gupta, A. (1996). Geometry and scaling
1410 relations of a population of very small rift-related normal faults. *Geology*, 24(8), 683.
1411 [https://doi.org/10.1130/0091-7613\(1996\)024<0683:GASROA>2.3.CO;2](https://doi.org/10.1130/0091-7613(1996)024<0683:GASROA>2.3.CO;2)

1412

1413